Universität
Münster

Maximilian Blümke

› Search for a Kinematic Anisotropy in the NANOGrav Data

2025

living.knowledge

institut für
theoretische physik

Universität
Münster

Search for a Kinematic Anisotropy in the NANOGrav Data

Bachelor thesis
submitted to the

Universität Münster
Institut für Theoretische Physik

by

Maximilian Blümke

September 2025

First examiner: Jun.-Prof. Dr. Kai Schmitz
Second examiner: Prof. Dr. Anna Kulesza

Day of submission: Sunday 14th September, 2025

Abstract

The North American Nanohertz Observatory for Gravitational Waves (NANOGrav) recently detected a $3-4\sigma$ significant evidence for the Stochastic Gravitational Wave background (SGWB). This result was obtained by measuring the two-point spatial correlation of timing residuals in the time of arrival (TOA) of pulses from an array of millisecond pulsars [1]. A crucial step towards this goal is the recovery of the Hellings-Downs curve (HDC) which is the theoretical prediction for the overlap reduction function (ORF) among pulsars given a certain angular separation ξ_{ab}. The classic HDC assumes an isotropic background; however anisotropies change the form of the expected ORF. Although previous general anisotropy searches have not found any significant evidence [2], a kinematic anisotropy induced by the Doppler shift that gravitational waves (GW) experience due to the motion of our rest frame to that in which the SGWB is isotropic is a guaranteed property. In this thesis, we search for kinematic anisotropies in the NANOGrav 15-year PTA dataset by using and expanding on the methods presented in [3]. We develop the mathematical framework necessary to quantify a kinematic dipole induced by the motion of the Solar System barycenter with respect to an isotropic rest frame, characterized by a dimensionless velocity parameter $\beta = v/c$. The formalism parallels that employed in studies of the kinematic dipole in the cosmic microwave background (CMB). We assume that the dipole is of the same order $\beta = \mathcal{O}(10^{-3})$ and direction [4] as the CMB dipole if the SGWB has a cosmological origin. We find analytical results for the ORF appearing up to the second order of β. Additional time is spent addressing the autocorrelation of the ORF, inspired by the work in [5]. Using a numerical Baysian analysis pipeline, we report different upper limits for β depending on the chosen model for the autocorrelation. Our results are summarized in table 3.1. In all cases, the results deviate from the one presented in [3].

Declaration of Academic Integrity

I hereby confirm that this thesis, entitled *Search for a Kinematic Anisotropy in the NANOGrav Data*, is solely my own work and that I have used no sources or aids other than the ones stated. All passages in my thesis for which other sources, including electronic media, have been used, be it direct quotes or content references, have been acknowledged as such and the sources cited. I am aware that plagiarism is considered an act of deception which can result in sanction in accordance with the examination regulations.

I consent to having my thesis cross-checked with other texts to identify possible similarities and to having it stored in a database for this purpose.

I confirm that I have not submitted the following thesis in part or whole as an examination paper before.

Münster, 14th September 2025

Maximilian Blümke

Contents

Introduction

1

One crucial milestone in understanding the universe is Einstein's General Relativity (GR), which describes the influence of energy and mass on the construct of spacetime itself. Similarly to electromagnetic waves, spacetime perturbations can take the form of propagating waves. A stochastic gravitational wave background (SGWB) arises from the superposition of numerous unresolved sources of gravitational waves, forming a kind of *background noise* in the universe that can be measured and analyzed. Recently, the NANOGrav collaboration reported a $3-4\sigma$ significance in the search for a gravitational wave background (GWB) by observing the correlation in the timing residuals of 67 pulsars [1]. Coinciding with the search for a GWB is the search for anisotropies within this background that could potentially reveal more about the origin of the GWB [2]. Currently, both astrophysical and cosmological origin models offer candidates for SGWB sources. Instead of focusing on the standard astrophysical explanation, this thesis assumes a cosmological origin of the GWB from early universe processes. A guaranteed property of this GWB model from a cosmological origin is a kinematic anisotropy due to the motion of our reference frame with respect to the rest frame in which the GWB is isotropic. The goal of this thesis is to find a kinematic dipole in the stochastic gravitational wave background and set an upper bound on the velocity $\beta = v/c$ of our solar system relative to the isotropic background following the work done in [3].

In order to understand many of the underlying concepts of this Bachelor thesis, we have a brief look into general relativity and how GWs develop using a geometric approach in section 2.1.1. GWs transport energy through spacetime, motivating the definition of an associated energy density parameter Ω_{SGWB} for the SGWB (section 2.1.2). In order to analyze the GWB we use pulsar timing array (PTA) experiments that make use of the unique attributes of pulsars discussed in section 2.2. By combining the properties of frequently observed pulsar pulses and how GWs affect them, we find in section 2.2.1 an equation for the time of arrival (TOA) for pulsar pulses under the influence of spacetime perturbations. In preparation for later considerations, two ways in which to define the energy density measured in PTA experiments are derived in section 2.2.2. Both are useful for later considerations. In the section 2.2.3 afterwards, we develop the necessary theory to recover the Hellings-Downs curve from pulsar timing arrays within an isotropic background, as usually done, which encompasses the angular dependence of the two-point correlation function between the timing residuals of two pulsars. By introducing a Doppler shift, the correlation is modified, and we will go on to explain the theoretical framework to recover β and introduce anisotropies (section 2.2.4). Our results for the overlap reduction function at quadratic order of β differ from the one presented in [3], therefore we will take dedicated time to discuss our own results. Unlike in other analyses, when taking into account the autocorrelation of the ORF we calculate the exact terms including the GW frequency and distance dependencies to the pulsars L_a (section 2.2.5). We also discuss other possible choices for the autocorrelation. To estimate the modification of the ORF due to the kinematic effect, we conduct a preliminary analysis using only pulsar positions (section 3.1). The following section 3.2 and section 3.3 revolve around the Bayesian analysis to numerically analyze PTA data using the Markov chain Monte Carlo algorithm to sample the posterior distribution. Our results are found in section 3.4. Lastly, we will discuss our results in the context of anisotropy searches within the GWB and explain how a CMB-independent analysis of the kinematic dipole amplitude and direction could provide valuable insights on the validity of ΛCDM (chapter 4). Three appendices supplement the thesis, providing detailed analytical derivations of the different overlap reduction functions arising from kinematic anisotropies (appendix A) and the Taylor expansion of the Doppler-shifted intensity (appendix B). Finally, appendix C contains the code for model files.

Henceforth, bold symbols like $\boldsymbol{n}$ will refer to vector objects and a hat $\hat{\boldsymbol{n}}$ a unit vector. If we refer to tensor components of different rank, we will refrain from using bold notation. The thesis uses the Einstein summation convention, where repeated indices are summed over (if not otherwise mentioned).

Mathematical Set-up

2

The following chapter is divided into two parts. In section 2.1 we discuss the basic derivation of Gravitational Waves from General Relativity using the geometric approach. The stochastic gravitational wave background is measured using Pulsar Timing Arrays, which we discuss in section 2.2.

2.1 Gravitational Waves

The Minkowski metric $\eta_{\mu\nu}$ describes flat four-dimensional spacetime [6]:

$$g_{\mu\nu} = \eta_{\mu\nu} \equiv \begin{pmatrix} -1 & 0 & 0 & 0 \\ 0 & 1 & 0 & 0 \\ 0 & 0 & 1 & 0 \\ 0 & 0 & 0 & 1 \end{pmatrix} . \tag{2.1}$$

In the following, $g_{\mu\nu}$ will refer to the total metric, consisting of the Minkowski metric $\eta_{\mu\nu}$ and a small perturbation $h_{\mu\nu}$ in spacetime:

$$g_{\mu\nu} = \eta_{\mu\nu} + h_{\mu\nu} \tag{2.2}$$

Also note that the metric performs an index raising or lowering when applied. In order to continue, we skip over some of the details leading to the Einstein equations, but introduce some of the symbols used to define it [7, 8]:

$$\partial_\mu = \frac{\partial}{\partial x^\mu} \equiv \left(\frac{1}{c}\partial_t, \partial_i \right) , \tag{2.3}$$

where c is the speed of light. Also of use are the Christoffel symbols

$$\Gamma^{\rho}_{\mu\nu} \equiv \frac{1}{2} g^{\rho\sigma} \left(\partial_\mu g_{\sigma\nu} + \partial_\nu g_{\sigma\mu} - \partial_\sigma g_{\mu\nu} \right), \tag{2.4}$$

the Riemann tensor

$$R^{\mu}{}_{\nu\rho\sigma} \equiv \partial_\rho \Gamma^{\mu}_{\nu\sigma} - \partial_\sigma \Gamma^{\mu}_{\nu\sigma} + \Gamma^{\mu}_{\alpha\rho} \Gamma^{\alpha}_{\nu\sigma} - \Gamma^{\mu}_{\alpha\sigma} \Gamma^{\alpha}_{\nu\rho}, \tag{2.5}$$

the Ricci tensor and Ricci scalar

$$R_{\mu\nu} \equiv R^{\alpha}{}_{\mu\alpha\nu} \tag{2.6}$$

$$R \equiv g^{\mu\nu} R_{\mu\nu}. \tag{2.7}$$

This culminates in the Einstein equations

$$G_{\mu\nu} \equiv R_{\mu\nu} - \frac{1}{2} g_{\mu\nu} R = \frac{8\pi G}{c^4} T_{\mu\nu}, \tag{2.8}$$

where $T^{\mu\nu}$ is the energy-momentum tensor of matter, G the gravitational constant, and c the speed of light. Without understanding the intricacies of this equation, one easily notices that it relates the distribution of matter (RHS) and the curvature of spacetime (LHS). From now on, we want to show that it can be rewritten as a wave equation, laying the mathematical groundwork for GWs.

2.1.1 Geometric Approach to Gravitational Waves

One of the more peculiar predictions of the general theory of relativity is the existence of gravitational waves. For the following analysis, we impose $|h_{\mu\nu}| \ll 1$. We expand to linear order (linearized theory) of $h_{\mu\nu}$ (truncating the rest) which gives [9]

$$G_{\mu\nu} = \frac{1}{2} \left(\partial_\mu \partial^\alpha h_{\alpha\nu} + \partial_\nu \partial^\alpha h_{\alpha\mu} - \partial_\mu \partial_\nu h - \Box h_{\mu\nu} + \eta_{\mu\nu} \Box h - \eta_{\mu\nu} \partial^\alpha \partial^\beta h_{\alpha\beta} \right), \tag{2.9}$$

where $h \equiv \eta^{\mu\nu} h_{\mu\nu}$ and $\Box \equiv \eta^{\mu\nu}\partial_\mu\partial_\nu$. In doing so, we have already assumed that the usual index lowering or raising can be performed using the Minkowski metric [9]. To clean up the notation, we introduce $\bar{h}_{\mu\nu} = h_{\mu\nu} - \eta_{\mu\nu}h/2$, so

$$\bar{h} \equiv \eta^{\mu\nu}\bar{h}_{\mu\nu} = h - 2h = -h \tag{2.10}$$

$$h_{\mu\nu} = \bar{h}_{\mu\nu} - \frac{1}{2}\eta_{\mu\nu}\bar{h}, \tag{2.11}$$

thus, equation (2.9) simplifies to [9]

$$G_{\mu\nu} = \frac{1}{2}\left(\partial_\mu\partial^\alpha\bar{h}_{\alpha\nu} + \partial_\nu\partial^\alpha\bar{h}_{\alpha\mu} - \Box\bar{h}_{\mu\nu} - \eta_{\mu\nu}\partial^\alpha\partial^\beta\bar{h}_{\alpha\beta}\right). \tag{2.12}$$

Similarly to electrodynamics, we introduce gauge conditions to identify degrees of freedom as presented in [8, 9, 10]. GR is invariant under the symmetry group of all possible coordinate transformations,

$$x^\mu \to x'^\mu(x), \tag{2.13}$$

as long as the transformation is a diffeomorphism [8]. The metric changes in the following way [8]:

$$g_{\mu\nu}(x) \to g'_{\mu\nu}(x') = \frac{\partial x^\rho}{\partial x'^\mu}\frac{\partial x^\sigma}{\partial x'^\nu}g_{\rho\sigma}(x). \tag{2.14}$$

Let us introduce the following change of coordinate systems $x^\mu \to x'^\mu = x^\mu + \xi^\mu$ where we assume the derivative of ξ to be small and observe the changes in the metric using equation (2.14) [8]:

$$\begin{aligned} g'_{\mu\nu}(x') &= \left(\delta_\mu{}^\rho - \frac{\partial\xi^\rho(x)}{\partial x'^\mu}\right)\left(\delta_\nu{}^\sigma - \frac{\partial\xi^\sigma(x)}{\partial x'^\nu}\right)g_{\rho\sigma}(x) \\ &= g_{\mu\nu}(x) - \left(\frac{\partial\xi_\nu(x)}{\partial x'^\mu} + \frac{\partial\xi_\mu(x)}{\partial x'^\nu}\right) + \mathcal{O}(\partial\xi\partial\xi) \\ &\approx g_{\mu\nu}(x) - \left(\frac{\partial\xi_\nu(x'-\xi)}{\partial x'^\mu} + \frac{\partial\xi_\mu(x'-\xi)}{\partial x'^\nu}\right) \\ &= g_{\mu\nu}(x) - \left(\partial_\mu\xi_\nu + \partial_\nu\xi_\mu\right) + \mathcal{O}(\xi\partial\xi) \\ &\approx g_{\mu\nu}(x) - \left(\partial_\mu\xi_\nu + \partial_\nu\xi_\mu\right). \end{aligned} \tag{2.15}$$

Invoking equation (2.2), we find

$$h_{\mu\nu}(x) \to h'_{\mu\nu}(x') = h_{\mu\nu}(x) - (\partial_\mu \xi_\nu + \partial_\nu \xi_\mu)\,, \tag{2.16}$$

which allows us to choose a gauge in which

$$\partial^\nu \bar{h}_{\mu\nu} = 0. \tag{2.17}$$

To prove that this is possible, consider equation (2.16) with the definitions introduced in equation (2.10) and equation (2.11), such that [8]

$$\bar{h}_{\mu\nu} \to \bar{h}'_{\mu\nu} = \bar{h}_{\mu\nu} - (\partial_\mu \xi_\nu + \partial_\nu \xi_\mu - \eta_{\mu\nu}\partial_\rho \xi^\rho)\,, \tag{2.18}$$

with

$$-\eta_{\mu\nu}\left(\frac{\bar{h}}{2} - \frac{\bar{h}'}{2}\right) = -\eta_{\mu\nu}\left(\frac{\eta^{\rho\sigma}}{2}(-h_{\rho\sigma} + h'_{\rho\sigma})\right) = \eta_{\mu\nu}\partial_\rho \xi^\rho, \tag{2.19}$$

from which follows

$$\partial^\nu \bar{h}_{\mu\nu} \to (\partial^\nu \bar{h}_{\mu\nu})' = \partial^\nu \bar{h}_{\mu\nu} - \Box \xi_\mu. \tag{2.20}$$

So, if the non-primed $h_{\mu\nu}$ does not fulfill the above declared gauge, we adjust $\Box\xi_\mu$ in a transformation accordingly. Using equation (2.12), we are left with the following expression that corresponds to a wave equation [9, 8]:

$$\Box \bar{h}_{\mu\nu} = -\frac{16\pi G}{c^4} T_{\mu\nu}. \tag{2.21}$$

Up to this point, the energy-momentum tensor had ten independent entries (since it is a symmetrical, 4×4 matrix), and through the introduction of the gauge, we reduced the degrees of freedom by four. For our observations, we are interested in propagating GWs with speed c outside their source, which is why we can set the RHS of equation (2.21) to zero. To further distill the degrees of freedom from the wave equation, the *transverse-traceless* (TT) gauge is introduced [9, 8]. Given that $\partial^\nu \bar{h}_{\mu\nu} = 0$, the condition is not affected by further transformations as long as $\Box\xi_\mu = 0$. This implies that

$$\Box \xi_{\mu\nu} \equiv \Box\,(\partial_\mu \xi_\nu + \partial_\nu \xi_\mu - \eta_{\mu\nu}\partial_\rho \xi^\rho) = 0, \tag{2.22}$$

as the four-dimensional, flat-space d'Alembertian $\Box$ commutes with ∂_μ. Therefore, $\xi_{\mu\nu}$ can be subtracted from $\bar{h}_{\mu\nu}$. $\xi_{\mu\nu}$ consists of four independent functions ξ_μ and satisfies $\Box\xi_{\mu\nu} = 0$. Choosing ξ^0 such that $\bar{h} = 0$ implies $\bar{h}_{\mu\nu} = h_{\mu\nu}$ given equation (2.11). The residual ξ^i can be fixed in such a way that $h^{0i}(x) = 0$. Observing equation (2.17) for $\mu = 0$ we find that $\partial^0 h_{00} = 0$, implying that h^{00} must now be constant in time [8]. Now, consider a gravitational potential in the Newtonian sense to be the source of the observed GWs. Naturally, one would attribute the time-independent properties of this system to the potential's source and the time-dependent properties to GWs. As we are outside the potential's source we can safely assume $h_{00} = 0$. Summarizing all the gauge changes made since,

$$h^{0\mu} = 0 \qquad\qquad h^i{}_i = 0 \qquad\qquad \partial^i h_{ij} = 0, \tag{2.23}$$

such that two degrees of freedom are left. To solve the wave equation in the transverse-traceless gauge, consider a single plane wave propagating along the z-axis [8, 9]:

$$h_{\mu\nu}(t,z) = \begin{pmatrix} 0 & 0 & 0 & 0 \\ 0 & h_+ & h_\times & 0 \\ 0 & h_\times & -h_+ & 0 \\ 0 & 0 & 0 & 0 \end{pmatrix} \cos\left[\omega(t - z/c)\right], \tag{2.24}$$

with the wave vector $k^\mu = (\omega/c, \boldsymbol{k})$, $\omega/c = |\boldsymbol{k}| = 2\pi f/c$ and the *plus* and *cross*-polarization h_+ and $h_\times$.

In the following, we are interested in the GW background that is defined by multiple GWs from all directions. Therefore, since $h_{0i} = 0$, the tensor can be reduced to the 3×3 matrix h_{ij}. The plane wave expansion for a GW in TT gauge can be written as an integral over all possible $\boldsymbol{k}$ [8]:

$$h_{ij}^{\mathrm{TT}}(\boldsymbol{x}) = \int \frac{d^3\boldsymbol{k}}{(2\pi)^3} \left(\mathcal{A}_{ij}(\boldsymbol{k}) e^{ik_\mu x^\mu} + \mathcal{A}_{ij}^*(\boldsymbol{k}) e^{-ik_\mu x^\mu}\right). \tag{2.25}$$

Changing into spherical coordinates, we get $d^3\boldsymbol{k} = (2\pi/c)^3 f^2 df\, d^2\hat{\boldsymbol{n}}$ where $\hat{\boldsymbol{n}}$ is the general unit propagation vector and f the frequency of the GW in Hertz:

$$h_{ij}^{\mathrm{TT}}(\boldsymbol{x}) = \frac{1}{c^3} \int_0^\infty df\, f^2 \int d^2\hat{\boldsymbol{n}}\, \left(\mathcal{A}_{ij}(f, \hat{\boldsymbol{n}}) e^{-2\pi i f(t - \hat{\boldsymbol{n}}\boldsymbol{x}/c)} + \mathrm{h.c.}\right). \tag{2.26}$$

Finally, we redefine our amplitudes to express them in terms of the polarization tensors $e^{\lambda}_{ij}(\hat{\boldsymbol{n}})$ and the Fourier-transformed perturbation amplitudes $\tilde{h}$ [8]:

$$\frac{f^2}{c^3}\mathcal{A}_{ij}(f,\hat{\boldsymbol{n}}) = \sum_{\lambda=+,\times} \tilde{h}_{\lambda}(f,\hat{\boldsymbol{n}})e^{\lambda}_{ij}(\hat{\boldsymbol{n}}). \tag{2.27}$$

The polarization tensors $e^{\lambda}_{ij}(\hat{\boldsymbol{n}})$ are useful quantities for later calculations. Given a plane wave expansion that propagates orthogonal to the unit vectors $\hat{\boldsymbol{u}}$ and $\hat{\boldsymbol{v}}$, they can be expressed in the following way [8]:

$$e^{+}_{ij}(\hat{\boldsymbol{n}}) = \hat{u}_i\hat{u}_j - \hat{v}_i\hat{v}_j \qquad\qquad e^{\times}_{ij}(\hat{\boldsymbol{n}}) = \hat{u}_i\hat{v}_j + \hat{v}_i\hat{u}_j, \tag{2.28}$$

and thus equation (2.26) becomes

$$h^{\mathrm{TT}}_{ij}(t,\boldsymbol{x}) = \sum_{\lambda=+,\times}\int_{-\infty}^{\infty} df \int d^2\hat{\boldsymbol{n}}\, \tilde{h}_{\lambda}(f,\hat{\boldsymbol{n}})e^{\lambda}_{ij}(\hat{\boldsymbol{n}})e^{-2\pi i f(t-\hat{\boldsymbol{n}}\boldsymbol{x}/c)}, \tag{2.29}$$

where $\tilde{h}_{\lambda}(-f,\hat{\boldsymbol{n}}) = \tilde{h}^{*}_{\lambda}(f,\hat{\boldsymbol{n}})$ was used. To make the polarization tensor more intuitive, figure 2.1 shows the effect of a propagating GW through a ring of beads.

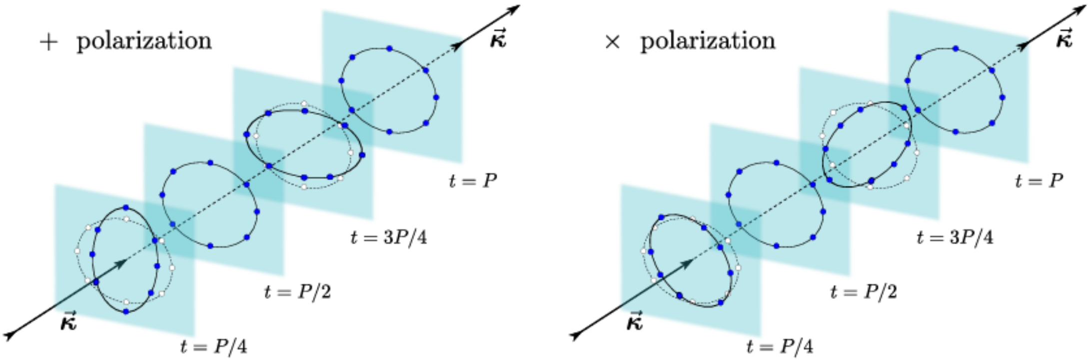

Figure 2.1: Given a ring of test particles, the effect of the two independent polarization tensors of a propagating GW is illustrated. Taken from [11].

2.1.2 Gravitational Wave Energy

GWs do in fact carry energy similar to electromagnetic waves. This can be simply concluded by imaging a bead on a string that is moved because a GW passes through it, creating friction [9]. Gravitational waves cannot be obscured like electromagnetic waves, since their interaction with other matter is much weaker and to source new GWs, extreme densities of matter or energy are needed. This makes them ideal messengers for otherwise inaccessible data in cosmology. Insights on their distribution are useful in understanding early universe processes and astrophysical massive objects in space [12].

How do we find the energy density? Assume a situation in which we can decompose the metric into a background $\bar{g}_{\mu\nu}$ and fluctuations $h_{\mu\nu}$ [8]:

$$g_{\mu\nu} = \bar{g}_{\mu\nu} + h_{\mu\nu}. \tag{2.30}$$

In order to do that, the background metric and perturbations have to have physical properties that set them apart. Firstly, the wavelength λ of the GW is much smaller than the spatial variation scale L_B of the background metric [8]:

$$\frac{\lambda}{2\pi} \ll L_B. \tag{2.31}$$

Alternatively, the frequency of the GW f is much higher than that of natural temporal variation f_B [8]:

$$f \gg f_B. \tag{2.32}$$

Expanding the Einstein equations in equation (2.8) up to order $\mathcal{O}(h^2)$

$$R_{\mu\nu} \approx \bar{R}_{\mu\nu} + R^{(1)}_{\mu\nu} + R^{(2)}_{\mu\nu}, \tag{2.33}$$

we know that $\bar{R}_{\mu\nu}$ can only be constructed using $\bar{g}_{\mu\nu}$ and $R^{(1)}_{\mu\nu}$ must be linear in $h_{\mu\nu}$. The first-order expansion contains high-frequency perturbations, given the condition from equation (2.32). $R^{(2)}_{\mu\nu}$ contains high and low frequency perturbations, since the wave vectors $\boldsymbol{k}$ can add up differently in frequency space. Given that, we rearrange the Einstein equations into low- and high-frequency parts (symbolized by the superscript) [8]:

$$\bar{R}_{\mu\nu} = -[R^{(2)}_{\mu\nu}]^{\mathrm{Low}} + \frac{8\pi G}{c^4}\left(T_{\mu\nu} - \frac{1}{2}g_{\mu\nu}T\right)^{\mathrm{Low}} \tag{2.34}$$

$$R^{(1)}_{\mu\nu} = -[R^{(2)}_{\mu\nu}]^{\mathrm{High}} + \frac{8\pi G}{c^4}\left(T_{\mu\nu} - \frac{1}{2}g_{\mu\nu}T\right)^{\mathrm{High}}. \tag{2.35}$$

Assuming that there is a separation between the length scales $\lambda/2\pi$ and L_B as in equation (2.31) we can carry out a spatial average over a volume with edge length l that is of an order in between the extremes ($\lambda/2\pi \ll l \ll L_B$) to receive the low-frequency GWs. For a separation of frequency as in equation (2.32) we can average over time t with $1/f \ll t \ll 1/f_B$. Thus, equation (2.34) can be written in the following way [8]:

$$\bar{R}_{\mu\nu} = -\langle R^{(2)}_{\mu\nu}\rangle + \frac{8\pi G}{c^4}\langle T_{\mu\nu} - \frac{1}{2}g_{\mu\nu}T\rangle, \tag{2.36}$$

where $\langle ... \rangle$ denotes the appropriate averaging process. We define a new quantity $t_{\mu\nu}$ as [8]

$$t_{\mu\nu} \equiv -\frac{c^4}{8\pi G}\langle R^{(2)}_{\mu\nu} - \frac{1}{2}\bar{g}_{\mu\nu}R^{(2)}\rangle. \tag{2.37}$$

The idea behind this equation is to observe only the influence of gravitational waves on the background metric with a tensor $t_{\mu\nu}$. We can now carry out the calculations, use the traceless transverse gauge for $R^{(2)}_{\mu\nu}$ and find that $\langle R^{(2)}\rangle$ vanishes, ending up with

$$t_{\mu\nu} = \frac{c^4}{32\pi G}\langle \partial_\mu h_{ij}\partial_\nu h^{ij}\rangle, \tag{2.38}$$

where the 00-component of the tensor corresponds to the gauge-invariant energy density ρ_{GW} [8].

Now, observing our universe, we expect a stochastic gravitational wave background that is essentially a summation of all spacetime perturbations propagating through space. At the low-frequency end of this background noise are gravitational waves from early universe processes like inflation, merely $10^{-32}\,\mathrm{s}$ after the big bang. In cosmology, energy density spectra are usually defined as a fraction of the critical energy density $\rho_c \equiv 3H_0^2/8\pi G$ which is the total energy density required for a flat geometry, where H_0 is the Hubble constant [9]:

$$\Omega_{\mathrm{SGWB}}(f) \equiv \frac{1}{\rho_c}\frac{d\rho_{\mathrm{SGWB}}}{d\ln f}. \tag{2.39}$$

Currently, there exists no conclusive measurement of the Hubble constant, the energy density is therefore given as $h_0^2\Omega_{\mathrm{SGWB}}$ with $H_0 = h_0\,100\,{}^{\mathrm{km}}\!/\!{}_{\mathrm{s\,Mpc}}$ [9].

2.2 Pulsar Timing Arrays

In order to measure GWs, we use the universe itself as a laboratory. More precisely, we make use of the properties of pulsars, a class of neutron stars that exhibit precise and predictable emission of radio waves. Pulsars form as a result of stellar collapse and conserve high amounts of angular momentum and magnetic flux [9]. From Maxwell's equations we know that rotating magnetic fields create a strong electric field. As a consequence, charged particles within the co-rotating magnetospheric plasma are accelerated and excite beams of measurable radio emissions [9, 13]. The dipole of the magnetic field is not aligned with the rotational axis, therefore the radiation beam rotates in space similar to a lighthouse [13]. The influence of this magnetic field reaches up to a *velocity-of-light cylinder* where an imagined extension of the pulsar's surface would at constant angular speed reach the speed of light. The situation is also illustrated in figure 2.2.

The pulse shape is rather stable (even though there is a loss of energy); therefore, we can identify deviations from this pattern as influences due to spacetime perturbations [9]. Before that, however, cosmologists need to account for several predictable influences on the radio frequencies. The exact procedure is quite complex and is not of interest for later considerations, so we will refrain from going into details. The ionized interstellar medium induces a frequency-dependent dispersion, which is corrected by considering the length of the path traveled by the signals from the pulsar to the detector [9]. After this correction, the pulses are integrated over and folded over the pulsar's estimated rotational period. The result is cross-correlated with a *template profile* for a specific pulsar [9]. The phase offset between the template and measured signals is saved as well as the time-of-arrival (TOA) data. We are mostly interested in the timing residuals. The time of arrival t_{TOA}

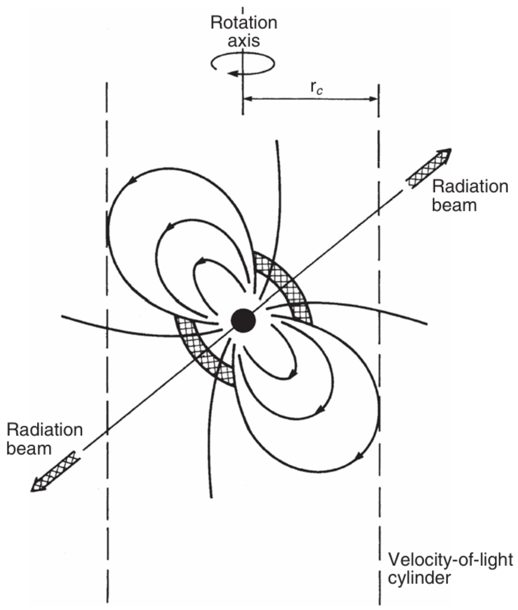

Figure 2.2: Illustrated are the features of a pulsar's magnetosphere in the lighthouse model. Notice the misalignment of the rotational axis and the radiation beam, which leads to an oscillation in the measurement of the emitted radio signals. The relevant radial distance r_c of the velocity-of-light cylinder is marked. Taken from [13].

and the emission time t_{PSR} from the pulsar are related through several corrections [9]:

$$t_{\text{PSR}} = t_{\text{TOA}} - \Delta_{\odot} - \Delta_{\text{IISM}} - \Delta_{B}, \tag{2.40}$$

where $\Delta_{\odot}$ is a timing correction from the detector position to the Solar System Barycenter (SSM), Δ_{IISM} is another correction because of propagation delays that account for varying interstellar dispersion and Δ_B which is a correction only for pulsars in binary systems [9]. The pulse phase of the pulsar is estimated with a least-squares fit that considers the loss of rotational momentum over time and is compared to the TOA; the difference is the timing residual. The timing residuals can now only be explained through detector noise and the desired GWs [9].

Now that we have discussed how PTA data is recorded and processed, we must study the effects of a GW on a timing residual. With that information, we identify the expected correlation of signals between different pulsars, the so-called Hellings-Downs curve (HDC). The HDC is calculated for an isotropic background; however, due to the movement of our Barycenter relative to the frame in which the background is isotropic, we expect the development of a kinematic dipole. The discussed model assumes that there exists a rest frame in which the SGWB is isotropic and that the movement of our measurement system is in the same direction and order of magnitude as that observed in cosmic microwave background (CMB) experiments. From CMB experiments, we expect that the magnitude of our velocity v is $\beta \equiv v/c = 1.23 \times 10^{-3}$ [3, 14, 15]. If this result could be confirmed with the SGWB, it could strengthen our current understanding of the early universe and validate searches of processes that describe GW production during this time, for example cosmic strings [16]. Another explanation for the SGWB is the superposition of orbiting supermassive black holes at the centers of galaxies [17]. Currently, PTA experiments do not have the sufficient sensitivity to resolve the anisotropy caused by their superposition (more on that in chapter 4). Nevertheless, through simulation and modeling we can set upper limits on β.

Differently from the previous chapter, we are now interested in more details. We will only work in TT gauge, thus we omit the superscript like in equation (2.29).

2.2.1 Effects of a Gravitational Wave

The metric of spacetime is perturbed by a gravitational wave

$$ds^2 = -c^2 dt^2 + \left[\delta_{ij} + h_{ij}(t, \boldsymbol{x}(t))\right] dx^i dx^j, \tag{2.41}$$

and photons traveling at the speed of light run along the null geodesic ($ds = 0$) such that we can expand the equation above to linear order of h_{ij} and integrate over, rearranging to

$$t_{\text{obs}} = t_{\text{em}} + \frac{L}{c} + \frac{\hat{x}^i \hat{x}^j}{2} \int_{t_{\text{em}}}^{t_{\text{em}}+L/c} dt'\, h_{ij}(t', (ct_{\text{em}} + L - ct')\hat{\boldsymbol{x}}), \tag{2.42}$$

where t_{em} is the pulse emission time, t_{obs} the observation time, L the pulsar-earth distance in TT gauge and finally $\hat{\boldsymbol{x}}$ the unit vector pointing from Earth to pulsar [16]. Normally, the proper upper bound of the integral should be t_{obs}. Though, it can be replaced with the unperturbed time for small h_{ij}; the same applies for the photon propagation. Now, consider another photon emitted in the same direction after a rotation of the pulsar with the period T, so the emission time is now $t'_{\text{em}} = t_{\text{em}} + T$.

Priming every quantity that indicates the photon emitted after the rotation, equation (2.42) changes to [16]

$$t'_{\text{obs}} = t_{\text{em}} + T + \frac{L}{c} + \frac{\hat{x}^i \hat{x}^j}{2} \int_{t_{\text{em}}}^{t_{\text{em}}+L/c} dt'\, h_{ij}(t' + T, (ct_{\text{em}} + L - ct')\hat{\boldsymbol{x}}), \tag{2.43}$$

and we can subtract this result from equation (2.42) to obtain

$$t'_{\text{obs}} - t_{\text{obs}} = T + \Delta T \tag{2.44}$$

with

$$\Delta T = \frac{\hat{x}^i \hat{x}^j}{2} \int_{t_{\text{em}}}^{\text{tem}+L/c} dt' \,\{h_{ij}(t' + T, (ct_{\text{em}} + L - ct')\hat{\boldsymbol{x}}) - h_{ij}(t', (ct_{\text{em}} + L - ct')\hat{\boldsymbol{x}})\}\,. \tag{2.45}$$

ΔT only encompasses the effects of GWs passing through the path of the photon [16]. T is the rotational period of the given pulsar, which is usually in millisecond order, while ω_{GW}, the frequency of the gravitational wave, is in the nanohertz spectrum [16]. We can therefore reasonably expand T within equation (2.45) up to the first order under the integral to obtain [16]

$$\frac{\Delta T}{T} = \frac{\hat{x}^i \hat{x}^j}{2} \int_{t_{\text{em}}}^{t_{\text{em}}+L/c} dt' \left[\frac{\partial}{\partial t'} h_{ij}(t', \boldsymbol{x})\right]_{\boldsymbol{x}=(ct_{\text{em}}+L-ct')\hat{\boldsymbol{x}}}. \tag{2.46}$$

2.2.2 Stochastic Gravitational Wave Background

Redefining our variables to $t \equiv t_{\text{em}} + L/c$, $z \equiv \Delta T/T$ and evaluating the now trivial integral using equation (2.29) gives [16]:

$$z(t) \equiv \sum_{\lambda=+,\times} \int_{-\infty}^{\infty} df \int d^2\hat{\boldsymbol{n}}\, \tilde{h}_\lambda(f, \hat{\boldsymbol{x}}) \frac{\hat{x}^i \hat{x}^j}{2(1 + \hat{\boldsymbol{n}}\hat{\boldsymbol{x}})} e^\lambda_{ij} e^{-2\pi i f t} \left[1 - e^{2\pi i f \frac{L}{c}(1+\hat{\boldsymbol{n}}\hat{\boldsymbol{x}})}\right], \tag{2.47}$$

which is the GW-induced redshift of the pulse arrival time. To simplify the notation, we introduce the detector tensor

$$D^{ij} \equiv \frac{\hat{x}^i \hat{x}^j}{2(1 + \hat{\boldsymbol{n}}\hat{\boldsymbol{x}})}. \tag{2.48}$$

A SGWB will be felt by all pulses, regardless of the measured pulsar. To *measure* the background we correlate two inputs from different measurements of pulsars. Owing to its statistical nature, only ensemble-averaged quantities can be meaningfully characterized, implying that the relevant statistical properties emerge from an average over many independent realizations of the system [8, 16]. However, it is impossible for us to observe multiple copies of our universe. In measurements, a temporal average denoted by $\langle ... \rangle$ is therefore used [8].

Our assumptions concern the mathematical attributes of the correlator of the Fourier transforms $\langle \tilde{h}_\lambda(f, \hat{\boldsymbol{n}}) \tilde{h}^*_{\lambda'}(f', \hat{\boldsymbol{n}}') \rangle$. Firstly, we expect the background to be stationary, meaning that any correlation cannot depend on absolute time. However, they can depend on relative time differences. In Fourier space this can be expressed as [8]

$$\langle \tilde{h}_\lambda(f, \hat{\boldsymbol{n}}) \tilde{h}^*_{\lambda'}(f', \hat{\boldsymbol{n}}') \rangle \propto \delta(f - f'). \tag{2.49}$$

In zeroth order (or the CMB rest frame as established previously), the stochastic background is also isotropic. We will account for the dipole anisotropy later, for now we consider that waves from different directions should be uncorrelated, so [8]

$$\langle \tilde{h}_\lambda(f, \hat{\boldsymbol{n}}) \tilde{h}^*_{\lambda'}(f', \hat{\boldsymbol{n}}') \rangle \propto \delta(\hat{\boldsymbol{n}} - \hat{\boldsymbol{n}}') \tag{2.50}$$

will suffice. As the background consists of the superposition of different GWs, it should also be unpolarized, leading to a factor of $\delta_{\lambda\lambda'}$ [8]. This attribute should be true for any of the SGWB origins (astrophysical or cosmological) [8]. After introducing a normalization and an f-dependent stochastic spectral intensity $I(f)$ we are left with [8]

$$\langle \tilde{h}_\lambda(f, \hat{\boldsymbol{n}}) \tilde{h}^*_{\lambda'}(f', \hat{\boldsymbol{n}}') \rangle = \frac{1}{8\pi} \delta(f - f') \delta(\hat{\boldsymbol{n}} - \hat{\boldsymbol{n}}') \delta_{\lambda\lambda'} I(f). \tag{2.51}$$

Normalization consists of a factor $1/4\pi$ for the integral over $\hat{\boldsymbol{n}}$ and $1/2$, since we will use a physical double-sided intensity. In order to understand $I(f)$, we compute the relation between $I(f)$ and Ω_{SGWB}. Using equation (2.29) and equation (2.51), where we drag the correlation brackets into the equation, the correlation with the time derivatives becomes

$$\langle \dot{h}_{ij}\dot{h}^{ij}\rangle = \frac{1}{8\pi}\sum_{\lambda}\int_{-\infty}^{\infty} df \int d^2\hat{\boldsymbol{n}}\,(2\pi f)^2 e^{\lambda}_{ij}e^{ij,\lambda}I(f) = 16\pi^2\int_{0}^{\infty} df\, f^2 I(f), \tag{2.52}$$

using the easily evaluated relation $\sum_{\lambda} e^{\lambda}_{ij}e^{\lambda,ij} = 4$ [8]. As in equation (2.39), we want to write the energy spectrum as a derivative of $\ln f$, hence

$$\rho_{\mathrm{GW}} \equiv \int_{0}^{\infty} df\,\frac{d\rho_{GW}}{df} = \int_{f=0}^{f=\infty} d\ln f\left(\frac{d\rho_{\mathrm{GW}}}{d\ln f}\right) \propto \int_{f=0}^{f=\infty} d\ln f\,\left(f^3 I(f)\right), \tag{2.53}$$

such that $\Omega_{\mathrm{SGWB}} \propto f^3 I(f)$ follows with equation (2.39) [8, 14]. For further calculations, we will also need a different approach to the energy density of the gravitational energy spectrum using the graviton number density per cell of phase space $\Delta(\boldsymbol{k})$ for a propagation vector $\boldsymbol{k}$. Because of isotropy, the density in phase space is only affected by $|\boldsymbol{k}| = \hbar\omega/c = hf/c$ and when integrating we can do that by using the infinitesimal sphere elements $d^3\boldsymbol{k} = (2\pi/c)^3 f^2 df\, d^2\hat{\boldsymbol{n}}$ [8, 14]. Once again, $\hat{\boldsymbol{n}}$ denotes the direction of propagation. The infinitesimal number of gravitons in a phase space element is therefore [8, 14]

$$dN = \Delta(f,\hat{\boldsymbol{n}})f^2 df\, d^2\hat{\boldsymbol{n}}dV. \tag{2.54}$$

Since the energy of a graviton is $\hbar\omega = hf$, the energy density can also be defined as

$$\rho_{\mathrm{GW}} \propto \int \frac{d^3\boldsymbol{k}}{(2\pi\hbar)^3}\Delta(f,\hat{\boldsymbol{n}})hf \propto \int d\ln f\,\Delta(f,\hat{\boldsymbol{n}})hf^4, \tag{2.55}$$

such that $\Omega_{\mathrm{SGWB}} \propto \Delta f^4$ [8]. This alternative approach towards understanding the energy density will be of importance later, since we will use the Lorentz invariance of the graviton number when shifting to the anisotropic viewpoint.

2.2.3 Hellings-Downs Curve

Going forward from the idea in the previous section, we compute the Hellings-Downs curve (HDC), which is the expected two-point correlator for the GWB given two pulsars (in general called overlap reduction function). Firstly, we want to look at the classic derivation of the HDC, but will quickly include our assumptions about the anisotropic kinematic dipole into our considerations. This will change the overlap reduction function significantly.

In the following, measurements from two different pulsars will be denoted by the index a and b. We compute the correlation of two redshifts from different pulsars at the same time, invoking equation (2.47)

$$\langle z_a(t) z_b(t)\rangle = \sum_{\lambda}\sum_{\lambda'}\int_{-\infty}^{\infty}\int_{-\infty}^{\infty} df\, df' \int\int d^2\hat{\boldsymbol{n}}\, d^2\hat{\boldsymbol{n}}' D_a^{\lambda}(\hat{\boldsymbol{n}}) D_b^{\lambda'}(\hat{\boldsymbol{n}}') \\ \left[1 - e^{2\pi i f \frac{L_a}{c}(1+\hat{\boldsymbol{n}}\hat{\boldsymbol{x}}_a)}\right]\left[1 - e^{-2\pi i f' \frac{L_b}{c}(1+\hat{\boldsymbol{n}}'\hat{\boldsymbol{x}}_b)}\right] e^{2\pi i (f-f')t}\langle h_{\lambda}(f,\hat{\boldsymbol{n}}) h^*_{\lambda'}(f',\hat{\boldsymbol{n}}')\rangle, \quad (2.56)$$

and applying equation (2.51), we are left with [16, 17]

$$\langle z_a(t) z_b(t)\rangle = \frac{1}{8\pi}\sum_{\lambda}\int_{-\infty}^{\infty} df \int d^2\hat{\boldsymbol{n}}\, D_a^{\lambda}(\hat{\boldsymbol{n}}) D_b^{\lambda}(\hat{\boldsymbol{n}}) \\ \left[1 - e^{2\pi i f \frac{L_a}{c}(1+\hat{\boldsymbol{n}}\hat{\boldsymbol{x}}_a)}\right]\left[1 - e^{-2\pi i f \frac{L_b}{c}(1+\hat{\boldsymbol{n}}\hat{\boldsymbol{x}}_b)}\right] I(f), \quad (2.57)$$

where

$$D_p^{\lambda} \equiv \frac{\hat{x}_p^i \hat{x}_p^j}{2(1+\hat{\boldsymbol{n}}\hat{\boldsymbol{x}}_p)} e_{ij}^{\lambda} \qquad p = a, b. \quad (2.58)$$

To further simplify equation (2.57), consider that the exponential terms in the squared brackets correspond to fast oscillating terms that, given the vast separation of two pulsars, vanish under the integral. Only in the case of two identical pulsars, henceforth referred to as the autocorrelation, the exponential terms multiply to

$$2 + \text{oscillating terms}, \quad (2.59)$$

such that one can reduce the squared brackets to [5]

$$1 + \delta_{ab}. \quad (2.60)$$

After introducing an arbitrary normalization, the HDC is defined as [16]

$$\Gamma_{ab}^{(0)} = (1+\delta_{ab})\,\frac{3}{8\pi}\int d^2\hat{\boldsymbol{n}}\,\sum_{\lambda} D_a^{\lambda}(\hat{\boldsymbol{n}}) D_b^{\lambda}(\hat{\boldsymbol{n}}), \quad (2.61)$$

which can be analytically calculated to (the lengthy calculation can be found in appendix A)

$$\Gamma^{(0)}_{ab} = (1+\delta_{ab})\left[\frac{1}{2} - \frac{1}{4}x_{ab} + \frac{3}{2}x_{ab}\ln x_{ab}\right], \tag{2.62}$$

where

$$x_{ab} \equiv \frac{1-\hat{\boldsymbol{x}}_a\hat{\boldsymbol{x}}_b}{2} \equiv \frac{1-\cos\xi_{ab}}{2}. \tag{2.63}$$

The HDC is only a function of the angular separation ξ_{ab} of the two pulsars and predicts the correlation produced by a set of non-interfering GW sources and its recovery is a strong hint at the existence of a SGWB [17]. One of the achievements of the North American Nanohertz Observatory for Gravitational Waves (NANOGrav) and their 15-year dataset is the report of a $3-4\sigma$ significance in the recovered HDC [1]. For the following calculations, we omit the factor $(1+\delta_{ab})$ and discuss approaches to the autocorrelation in the section afterwards.

2.2.4 Kinematic Anisotropy

We try to derive the correction of the overlap reduction function with the inclusion of the kinematic dipole that exists in the data due to the relative motion of the earth's rest frame to that of the universe, which we assume to be identical to that of the Cosmic Microwave Background (CMB) in the case of a cosmological origin. The analysis is largely inspired by the treatment in [3, 14, 15]. The velocity is expected to be $\beta = v/c = 1.23\cdot 10^{-3}$ [3, 4, 15]. As discussed in [18], this kinematic dipole has to be a superposition of two different effects: The movement of the solar system to the SGWB rest frame, which we do not expect to vary significantly over our measured timescales and the earth's annual movement around the solar barycenter. Although the second effect does contribute a yearly varying dipole, its magnitude is small compared to that of the first one, which is why we focus on the solar kinematic dipole. Later on, we want to reconsider our approach towards the autocorrelation of the timing residuals of the same pulsar. First, we introduce the isotropic GW intensity [3]:

$$\bar{I}(f) = \frac{1}{4\pi}\int d^2\hat{\boldsymbol{n}}\, I(f,\hat{\boldsymbol{n}}). \tag{2.64}$$

Beforehand, we assumed that $I(f)$ was only dependent on frequency, now consider it also depending on $\hat{\boldsymbol{n}}$ as it develops anisotropies. The integral to evaluate the HDC is defined as

$$\Gamma_{ab} = \frac{3}{8\pi} \int d^2\hat{\boldsymbol{n}} \sum_{\lambda} D_a^{\lambda}(\hat{\boldsymbol{n}}) D_b^{\lambda}(\hat{\boldsymbol{n}}) \\ \left[1 - e^{2\pi i f \frac{L_a}{c}(1+\hat{\boldsymbol{n}}\hat{\boldsymbol{x}}_a)}\right] \left[1 - e^{-2\pi i f \frac{L_b}{c}(1+\hat{\boldsymbol{n}}\hat{\boldsymbol{x}}_b)}\right] \frac{I(f,\hat{\boldsymbol{n}})}{\bar{I}(f)}; \quad (2.65)$$

notice the introduced normalization. All of our following considerations are made using the assumption that a kinematic anisotropy develops in the PTA experiments due to a velocity vector $\boldsymbol{v}$ and a corresponding Doppler boost [14]. This can be intuitively understood by imagining an isotropic radiation of light from the center of a chosen system. Moving with a velocity in one direction, the radiation in front of us (which we are moving towards) is blue-shifted, while the one that emits from behind us is red-shifted. This is a very simplified understanding of what the cause of the CMB dipole is. We will extend our considerations to the SGWB now. We define the transformation of frequency due to a Doppler shift as $\mathcal{D}$. Assume $\mathcal{S}'$ to be the frame in which the SGWB is isotropic. In a moving frame $\mathcal{S}$ a wave with frequency f and unit propagation vector $\hat{\boldsymbol{n}}$ shifts according to [14, 15]

$$\mathcal{D} = \frac{\sqrt{1-\beta^2}}{1-\beta\hat{\boldsymbol{n}}\hat{\boldsymbol{v}}} \quad (2.66)$$

$$f = \mathcal{D} f', \quad (2.67)$$

where $\beta \equiv v/c$ and $\hat{\boldsymbol{v}}$ is the unit vector of the velocity. Changing into the frame in which the SGWB is isotropic, the intensity becomes isotropic $I(f,\hat{\boldsymbol{n}}) \to \bar{I}(f)$. We find the transformation for $I(f,\hat{\boldsymbol{n}})$ by using the invariance of the graviton number discussed in the derivation of the energy density with gravitons in equation (2.54) [14]

$$dN' = dN. \quad (2.68)$$

Using $df' = \mathcal{D}^{-1}df$, $d^2\hat{\boldsymbol{n}}' = \mathcal{D}^2 d^2\hat{\boldsymbol{n}}$, $dV' = \mathcal{D}dV$ (from [19]) and equation (2.54), the following statement must be true

$$\Delta'(f',\hat{\boldsymbol{n}}') = \Delta(f,\hat{\boldsymbol{n}}). \quad (2.69)$$

Previously, we found $\Delta \propto f^{-4}\Omega_{\rm GW}$ in equation (2.55), so one can find the transformation of the density parameter [14]

$$\Omega_{\rm GW}(f,\hat{\boldsymbol{n}}) = \left(\frac{f}{f'}\right)^4 \Omega'_{\rm GW}(f',\hat{\boldsymbol{n}}') = \mathcal{D}^4\Omega'_{\rm GW}(f',\hat{\boldsymbol{n}}'). \tag{2.70}$$

If the statistical gravitational wave background has a rest frame in which it is isotropic (so no intrinsic anisotropies), the $\hat{\boldsymbol{n}}$ dependence of $I(f,\hat{\boldsymbol{n}})$ discussed above develops solely because of the introduction of $\mathcal{D}$ for the frequency Doppler shift. This step is very crucial to understand and special to the discussion presented in [15]. Previous PTA anisotropy searches used a product ansatz $I(f,\hat{\boldsymbol{n}}) = I(f)P(\hat{\boldsymbol{n}})$ and developed $P(\hat{\boldsymbol{n}})$ in terms of spherical harmonics (for example, in [2]). However, in our case $(f,\hat{\boldsymbol{n}}) \to (\mathcal{D}^{-1}f)$. Using the dependence $I \propto \Omega f^{-3}$ in equation (2.53) [15]

$$\begin{aligned}\frac{I(f,\hat{\boldsymbol{n}})}{\bar{I}(f)} = \mathcal{D}\frac{\bar{I}(\mathcal{D}^{-1}f)}{\bar{I}(f)} &= \left[1 - \frac{\beta^2}{6}(1-n_I^2-\alpha_I)\right] + \beta(1-n_I)\hat{\boldsymbol{n}}\hat{\boldsymbol{v}} \\ &+ \frac{\beta^2}{2}\left((\hat{\boldsymbol{n}}\hat{\boldsymbol{v}})^2 - \frac{1}{3}\right)(2-3n_I+n_I^2+\alpha_I) + \mathcal{O}(\beta^3),\end{aligned} \tag{2.71}$$

where in the last step, we extend up to the second order of β. In reference to the CMB we use the definition

$$n_I \equiv \frac{d\ln \bar{I}}{d\ln f} \qquad\qquad \alpha_I \equiv \frac{dn_I}{d\ln f}. \tag{2.72}$$

The full Taylor expansion can be found in appendix B. As one can see, we get a dipole term that deviates from the usual HDC, by complicating the integral with a factor of $\hat{\boldsymbol{n}}\hat{\boldsymbol{v}}$ and a term that scales with $(\hat{\boldsymbol{n}}\hat{\boldsymbol{v}})^2$. For the case of two different pulsars, the oscillating terms in the squared brackets of equation (2.65) vanish upon integration, due to their high frequency, leaving us with the following [3]:

$$\begin{aligned}\Gamma_{ab} = \left[1 - \frac{\beta^2}{6}(1-n_I^2-\alpha_I)\right]\Gamma_{ab}^{(0)} &+ \beta(1-n_I)\Gamma_{ab}^{(1)} \\ &+ \frac{\beta^2}{2}(2-3n_I+n_I^2+\alpha_I)\Gamma_{ab}^{(2)}\end{aligned} \tag{2.73}$$

Using contour integration, we can evaluate the integrals ($x_{ab} = (1 - \hat{\boldsymbol{x}}_a \hat{\boldsymbol{x}}_b)/2$) (we also used a different normalization of the HDC which differs by a factor of $3/2$ from that found in [3], but made sure to change it accordingly in every following example) [20]:

$$\Gamma^{(0)}_{ab} = \frac{1}{2} - \frac{x_{ab}}{4} + \frac{3}{2} x_{ab} \ln x_{ab} \tag{2.74}$$

$$\Gamma^{(1)}_{ab} = \left(-\frac{1}{8} - \frac{3}{4} x_{ab} - \frac{3 x_{ab} \ln x_{ab}}{4\,(1 - x_{ab})} \right) \left[\hat{\boldsymbol{v}} \hat{\boldsymbol{x}}_a + \hat{\boldsymbol{v}} \hat{\boldsymbol{x}}_b \right]. \tag{2.75}$$

In [15, 3] the result

$$\begin{aligned} \Gamma^{(2)}_{ab} = \frac{3}{2} \left(\frac{3 - 13 x_{ab}}{20(x_{ab} - 1)} + \frac{x_{ab}^2 \ln x_{ab}}{2(1 - x_{ab})^2} \right) \left[(\hat{\boldsymbol{v}} \hat{\boldsymbol{x}}_a)(\hat{\boldsymbol{v}} \hat{\boldsymbol{x}}_b) \right] \\ + \left(\frac{1 + 2x_{ab} - 4x_{ab}^2 + x_{ab}^3 + 3 x_{ab} \ln x_{ab}}{8(1 - x_{ab})^2} \right) \left[(\hat{\boldsymbol{v}} \hat{\boldsymbol{x}}_a)^2 + (\hat{\boldsymbol{v}} \hat{\boldsymbol{x}}_b)^2 \right] \end{aligned} \tag{2.76}$$

for the quadrupole contributions of the order β^2 is presented that involves the integral over $((\hat{\boldsymbol{n}} \hat{\boldsymbol{v}})^2 - 1/3)$. We could not reproduce the results presented. Again, the full analytical derivation of our analysis can be found in appendix A:

$$\begin{aligned} \Gamma^{(2)}_{ab} = \frac{1}{(x_{ab} - 1)^2} \Bigg\{ \left(\frac{1}{4} x_{ab}^3 - x_{ab}^2 + \frac{3}{4} x_{ab} \ln x_{ab} + \frac{1}{2} x_{ab} + \frac{1}{4} \right) \left[(\hat{\boldsymbol{v}} \hat{\boldsymbol{x}}_a)^2 + (\hat{\boldsymbol{v}} \hat{\boldsymbol{x}}_b)^2 \right] \\ + \left(\frac{3}{2} x_{ab}^2 \ln x_{ab} - \frac{39}{20} x_{ab}^2 + \frac{12}{5} x_{ab} - \frac{9}{20} \right) \left[(\hat{\boldsymbol{v}} \hat{\boldsymbol{x}}_a)(\hat{\boldsymbol{v}} \hat{\boldsymbol{x}}_b) \right] \\ + \left(x_{ab}^3 \ln x_{ab} - \frac{22}{15} x_{ab}^3 - \frac{1}{2} x_{ab}^2 \ln x_{ab} + \frac{35}{12} x_{ab}^2 - \frac{1}{2} x_{ab} \ln x_{ab} - \frac{43}{30} x_{ab} - \frac{1}{60} \right) \Bigg\}. \end{aligned} \tag{2.77}$$

We briefly take the time to comment on the differences regarding our evaluation of

$$\Gamma^{(2)}_{ab} = \frac{3}{8\pi} \int d^2 \hat{\boldsymbol{n}} \sum_{\lambda} D^{\lambda}_a D^{\lambda}_b \left[(\hat{\boldsymbol{n}} \hat{\boldsymbol{v}})^2 - \frac{1}{3} \right] \tag{2.78}$$

and the one presented in [3]. For the remaining thesis, we will use our solution (unless otherwise mentioned). For a consistency check, consider an orthogonal system, in which we fix the pulsar orientation in the xz-plane and the velocity along the y-axis. Using the calculations presented in appendix A and the appendix of [20] we find

$$\frac{3}{16\pi}\int_{-1}^{1} dx \int_{0}^{2\pi} d\phi \left[(1-x^2)\sin^2\phi - \frac{1}{3}\right]\frac{1}{2}(1-x) \left[(1 - x\cos\xi - \sqrt{1-x^2}\sin\xi\cos\phi) - \frac{2\sin^2\xi\sin^2\phi}{1+x\cos\xi+\sqrt{1-x^2}\cos\phi}\right]. \quad (2.79)$$

For a short numerical evaluation using `Wolfram Mathematica`, we stick to the case of $\xi = \pi/2$ which is the case for pulsars along the x and z-axis

$$\frac{3}{16\pi}\int_{-1}^{1} dx \int_{0}^{2\pi} d\phi \left[(1-x^2)\sin^2\phi - \frac{1}{3}\right]\frac{1}{2}(1-x) \left[(1 - \sqrt{1-x^2}\cos\phi) - \frac{2\sin^2\phi}{1+\sqrt{1-x^2}\cos\phi}\right] \approx -0.0568528, \quad (2.80)$$

which matches our result in equation (2.77). In contrast, equation (2.76) vanishes because of the dot products. To illustrate this argument, refer to figure 2.3. Clearly, the contributions for $\Gamma_{ab}^{(2)}$ do not vanish fully in the system in which the velocity is orthogonal to the pulsar plane. With the exception of the $-1/3$ contribution in equation (2.78), the integral is dependent on $\hat{\boldsymbol{n}}\hat{\boldsymbol{v}}$. After integrating over $\hat{\boldsymbol{n}}$, only dot product combinations of $\hat{\boldsymbol{v}}$, $\hat{\boldsymbol{x}}_a$, and $\hat{\boldsymbol{x}}_b$ are possible. Given our result for the orthogonal velocity vector, the solution must therefore include contributions that are proportional to $(\hat{\boldsymbol{v}}\hat{\boldsymbol{v}})(\hat{\boldsymbol{x}}_a\hat{\boldsymbol{x}}_a)$ and $(\hat{\boldsymbol{v}}\hat{\boldsymbol{v}})(\hat{\boldsymbol{x}}_b\hat{\boldsymbol{x}}_b)$ and, as such, do not vanish in the special case.

2.2.5 Different cases for the Autocorrelation

The autocorrelation in [3] is simply set to unity (although not explicitly stated, we discovered this during testing). However, a more reasonable approach is to take the limit $x_{ab} \to 0$ and consider the factor $1 + \delta_{ab}$. Up to β^2 contributions equation (2.73) reduce to

$$\Gamma_{aa} = \left[1 - \frac{\beta^2}{6}\left(1 - n_I^2 - \alpha_I\right)\right] + \frac{1}{2}\beta(n_I - 1)\left[\hat{\boldsymbol{v}}\hat{\boldsymbol{x}}_a\right] + \frac{\beta^2}{2}\left(2 - 3n_I + n_I^2 + \alpha_I\right)\left(\frac{1}{10}\left[\hat{\boldsymbol{v}}\hat{\boldsymbol{x}}_a\right]^2 - \frac{1}{30}\right). \quad (2.81)$$

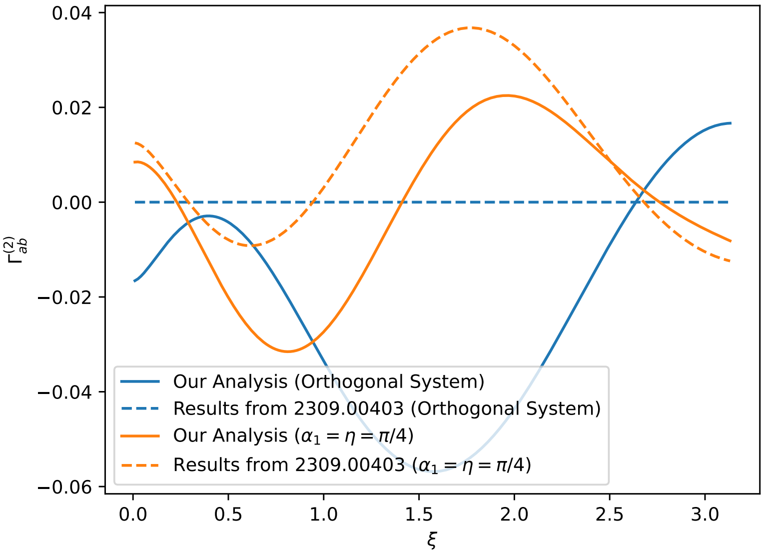

Figure 2.3: Comparison of the solutions for the $\Gamma_{ab}^{(2)}$ contributions from the paper [3] and our analysis (we made sure to adjust the normalization). The blue lines indicate a system in which the vectors of the pulsar location are in a plane orthogonal to the velocity while the orange plot is in the case of $\alpha_1 = \eta_1 = \pi/4$ (angles for $\hat{\boldsymbol{v}}$, see appendix A).

At this point, we also want to consider a different approach to the autocorrelation, since we are already making corrections at order $\mathcal{O}(10^{-3})$, following the ideas presented in [5]. For the case of two identical pulsars $x_{ab} \to 0$, but we can no longer omit the oscillating terms in equation (2.65):

$$\Gamma_{aa} = \frac{3}{8\pi} \int d^2\hat{\boldsymbol{n}} \sum_{\lambda} \left(D_a^\lambda(\hat{\boldsymbol{n}})\right)^2 \left[1 - e^{2\pi i f \frac{L_a}{c}(1+\hat{\boldsymbol{n}}\hat{\boldsymbol{x}}_a)}\right] [\text{h.c.}]$$
$$\left(\left(1 - \frac{\beta^2}{6}(1 - n_I^2 - \alpha_I)\right) + \beta(1-n_I)\hat{\boldsymbol{n}}\hat{\boldsymbol{v}} + \frac{\beta^2}{2}\left((\hat{\boldsymbol{n}}\hat{\boldsymbol{v}})^2 - \frac{1}{3}\right)(2 - 3n_I + n_I^2 + \alpha_I)\right). \tag{2.82}$$

For simplicity, we will now set $c = 1$. We adopt the same alignment of equations as in equation (2.73) and receive for the monopole contribution [5]:

$$\Gamma_{aa}^{(0)} = 1 - \frac{3\left[1 - \text{sinc}(4\pi f L_a)\right]}{8(\pi f L_a)^2} \tag{2.83}$$

In order to do the correction of the auto correlation that is within the linear order of β, we fix the pulsar direction along the z-axis. The velocity unit vector $\hat{\boldsymbol{v}}$ lies within the xz-plane where α describes the angle between the measured pulsar and the velocity vector of our moving reference frame:

$$\hat{\boldsymbol{n}}\hat{\boldsymbol{x}}_a = \cos\theta \qquad\qquad \hat{\boldsymbol{n}}\hat{\boldsymbol{v}} = \cos\alpha\cos\theta + \sin\alpha\sin\theta\cos\phi \tag{2.84}$$

For this case, the detection tensors become (refer to equation (A.13) from appendix A):

$$\sum_\lambda (D_a^\lambda)^2 = \frac{1}{4}\left(1-\cos\theta\right)^2 . \tag{2.85}$$

Plugging everything into the dipol autocorrelation function:

$$\begin{aligned}
\Gamma_{aa}^{(1)} &= \frac{3}{8\pi}\int d^2\hat{\boldsymbol{n}}\ \left[2-2\cos(2\pi f L_a(1+\hat{\boldsymbol{n}}\hat{\boldsymbol{x}}_a))\right]\left[\hat{\boldsymbol{n}}\hat{\boldsymbol{v}}\right]\frac{1}{4}\left(1-\cos\theta\right)^2 \\
&= \frac{3}{8\pi}\int_0^\pi\int_0^{2\pi} d\phi\, d\theta\ \sin\theta\left[2-2\cos(2\pi f L_a(1+\cos\theta))\right] \\
&\left[\cos\alpha\cos\theta+\sin\alpha\sin\theta\cos\phi\right]\frac{1}{4}\left(1-\cos\theta\right)^2 \\
&= \frac{3}{4}\int_0^\theta d\theta\ \sin\theta\left[1-\cos(2\pi f L_a(1+\cos\theta))\right]\left[\cos\alpha\cos\theta\right]\frac{1}{2}\left(1-\cos\theta\right)^2 \\
&= \frac{3}{8}\cos\alpha\int_{-1}^{1} dx\ \left[1-\cos(2\pi f L_a(1+x))\right]x\left(1-x\right)^2 \\
&= \left(-\frac{1}{2}+\frac{3}{4(\pi f L_a)^2}+\frac{3\sin(4\pi f L_a)}{32(\pi f L_a)^3}+\frac{9(\cos(4\pi f L_a)-1)}{64(\pi f L_a)^4}\right)\cos\alpha.
\end{aligned} \tag{2.86}$$

The same same approach can be used for $\Gamma_{aa}^{(2)}$

$$\Gamma_{aa}^{(2)} = \frac{3}{8\pi}\int d^2\hat{\boldsymbol{n}}\left[2-2\cos(2\pi f L_a(1+\hat{\boldsymbol{n}}\hat{\boldsymbol{x}}_a))\right]\left[(\hat{\boldsymbol{n}}\hat{\boldsymbol{v}})^2-\frac{1}{3}\right]\frac{1}{4}(1-\cos\theta)^2, \tag{2.87}$$

which evaluates to

$$\begin{aligned}\Gamma_{aa}^{(2)} = \frac{1}{1280(\pi f L_a)^5}\Bigg[&64(\pi f L_a)^5 \cos(2\alpha) + \frac{64(\pi f L_a)^5}{3} - 960(\pi f L_a)^3 \cos(2\alpha)\\ &- 320(\pi f L_a)^3 + 20(\pi f L_a)^2 \sin(4\pi f L_a) - 30(\pi f L_a)^2 \sin(2\alpha - 4\pi f L_a)\\ &+ 30(\pi f L_a)^2 \sin(2\alpha + 4\pi f L_a) + 2160\pi f L_a \sin^4(\pi f L_a)\cos(2\alpha)\\ &+ 720\pi f L_a \sin^4(\pi f L_a) + 360\pi f L_a \cos(2\pi f L_a) + 540\pi f L_a \cos(2\alpha - 2\pi f L_a)\\ &+ 540\pi f L_a \cos(2\alpha + 2\pi f L_a) - 90\sin(4\pi f L_a) + 135\sin(2\alpha - 4\pi f L_a)\\ &- 135\sin(2\alpha + 4\pi f L_a)\Bigg]. \qquad (2.88)\end{aligned}$$

For $fL_a \to \infty$ these match the result in equation (2.81). The goal of this Bachelor thesis is to find an upper bound on β by using experimental data and our mathematical analysis in this section.

3

Analysis with PTA Data

In the first section of this chapter, the ORF and its capability to respond to the kinematic dipole are analyzed as a forecast by using the location of the pulsars used by NANOGrav in the 15-year dataset. To understand how the experimental data are being processed, we quickly dive into Bayesian statistics. After that, the numerical processes are briefly explained, and the results of our analysis are presented.

3.1 Preliminary Analysis

Before starting with the numerical analysis, we should consider the pulsar locations and how they are oriented to the velocity vector. In figure 3.1 we observe that the 67 pulsars considered for the NANOGrav 15-year dataset are not evenly distributed across the celestial sphere. Given the dot product in the square brackets of equation (2.75), one may easily assume that pulsars that are mostly along the velocity vector are sensitive to the kinematic dipole (dark colored dots in figure 3.1). In figure 3.2, the ORF for different values of β can be observed. The ORF was constructed using the 67 pulsars. The scattered dots are all possible two-point correlators. Each dot represents a unique pairing of pulsars. Roughly, the shape of the HDC is preserved. The dot products for two different pulsar combinations can add up differently (because of their individual position), resulting in different ORF values at the same angular separation. The evaluated ORF for two pulsars near the dipole are marked in a darker tone. They indicate that while they contribute to significant deviations from the HDC (see dark dots at smaller angular separation), especially in the middle region of the ORF, sizable differences are observed. The correlation is therefore sensitive to kinematic anisotropies at a reasonable scale even if not all pulsars are located near the dipole direction.

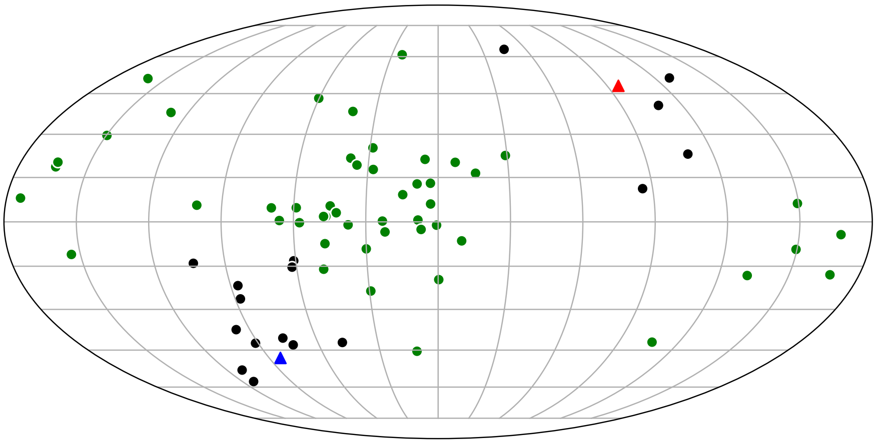

Figure 3.1: 67 pulsars monitored by the NANOGrav collaboration in galactic coordinates and mapped using a Mollweide projection. The velocity vector as determined by the CMB reaches from the blue to the red triangle (in galactic coordinates $(l, b) = (264^\circ, 48^\circ)$) [4]. Pulsars that we expect to have a high sensitivity (within a 40° circular boundary of the dipole direction) to the dipole are colored black. The data for this analysis is taken from [21] and their recent data can be found at `https://www.atnf.csiro.au/research/pulsar/psrca`.

3.2 Bayesian Statistics

When we think about measuring something in physics, we often use frequentist statistics. Suppose that we try to measure the physical quantity with the true value x_t. Instead, we measure x_0. Due to imperfect measurement, we can never truly observe x_t. Rather through repeated observations, we can construct intervals that, given an ensemble of repeated experiments, contain x_t up to a certain confidence level [22]. In cosmology, this approach is questionable, since phenomena like merging black holes or strong GWs can only be measured once. Therefore, a Bayesian approach is often used. Consider a probability distribution $p(d|\theta, \mathcal{H})$. This is called a likelihood function and is the probability of finding some specific data d given a

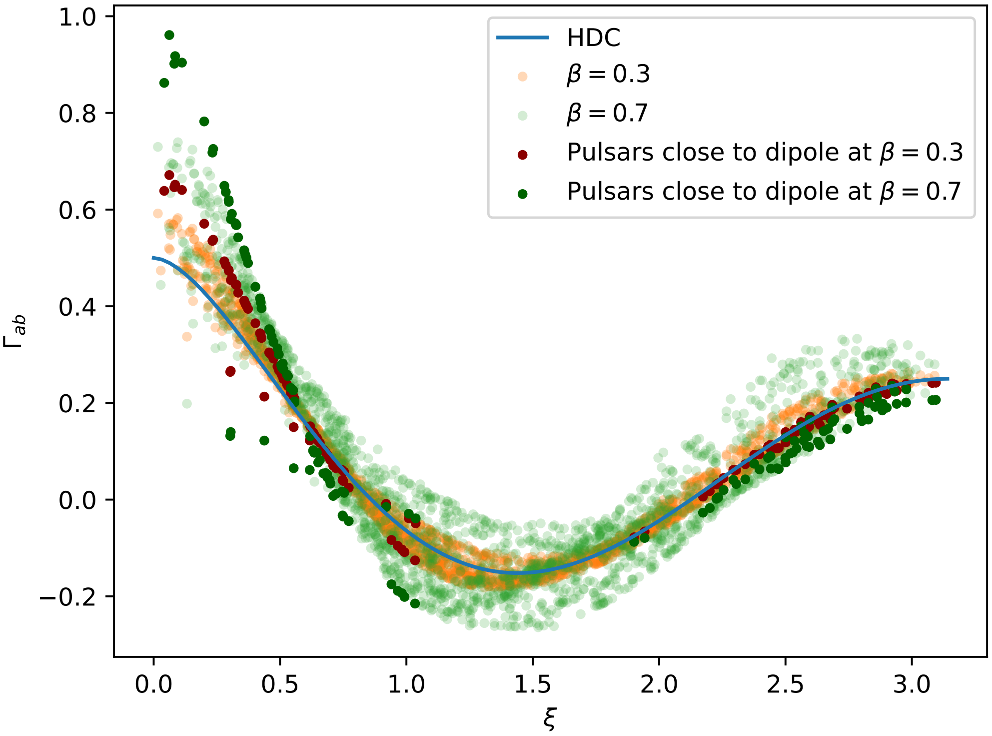

Figure 3.2: The blue line indicates the HDC (essentially the case for $\beta = 0$). Using the pulsar catalog by [21] we create a scatter plot for different levels of β to observe the influence of the dot product contributions on the ORF. Interestingly, deviations in the HDC are not solely caused by pulsar pairs near the dipole (which were colored in a slightly darker color). For this case, typical values for a power-law of $n_I = -1.33$ and $\alpha_I = 0$ were chosen.

set of parameters θ that belong to a hypothesis $\mathcal{H}$. Bayes' Theorem allows us to construct a probability distribution of parameters given some data

$$p(\theta|d) = \frac{p(d|\theta)p(\theta)}{p(d)}, \tag{3.1}$$

where we call $p(\theta|d)$ the posterior probability distribution and $p(\theta)$ the prior probability of θ [8, 9]. From a Bayesian viewpoint, probability is a measure of belief that is updated by data. There is no *true* value x_t but rather the measurement and the model parameters derived from that. The prior can be constructed using our knowledge from the physical analysis while $p(d)$ is part of the normalization. In the case of multiple parameters, marginalization is performed [9]

$$p(x|d) = \int dydz\, p(x, y, z|d) \tag{3.2}$$

to find single-parameter posteriors. To construct intervals within credible levels, we integrate over the area that is enclosed by the posterior distribution. Consider a one-dimensional arbitrary normalized posterior distribution. We integrate over the region that is enclosed by the leftmost and rightmost intersection between a horizontal line lowered from the highest posterior distribution value and the posterior distribution [9]. The credible level indicates the posterior probability mass that is contained in this interval. For multiple parameters, we use corner plots to show the posterior distribution of different parameters. In the diagonal plots, parameters are marginalized over. In many cases, it is useful to compare two models through the so-called Bayes factor

$$\mathcal{B} = \frac{\mathcal{Z}_1}{\mathcal{Z}_2}, \tag{3.3}$$

with

$$\mathcal{Z}_i = \int p(d|\theta_i)p(\theta_i)d^n\theta, \tag{3.4}$$

where $\theta = (\theta_1, \ldots, \theta_n)$ [9, 23].

3.3 Numerical Methods

In this section, the numerical analysis methods used in this thesis are briefly presented. The PTA likelihood is constructed using the timing residuals $\vec{\delta t}$. They are the remaining difference between the assumed and measured pulsar pulse time of arrival, which consist of white noise $\vec{n}$, red noise, and errors from the fit of the pulsar model $\vec{\epsilon}$(for arrays of data we will use the vector arrow notation and the matrices will be written bold, differently from what was done before) [23, 24]:

$$\vec{\delta t} = \vec{n} + \boldsymbol{F}\vec{a} + \boldsymbol{M}\vec{\epsilon}, \tag{3.5}$$

where $\boldsymbol{F}$ and $\boldsymbol{M}$ are matrices. White noise $\vec{n}$ is a zero-mean, normal random variable [23]. $\boldsymbol{F}$ is the Fourier design matrix that contains a set of sine and cosine pairs evaluated at different observation times for a Fourier basis with frequencies i/T_{obs} where T_{obs} is the total observation time. The specific coefficients of the sine and cosine terms are found in $\vec{a}$ that should contain the intrinsic red noise component of the pulsar and the GW-induced shift. They are assumed to be normal distributed zero-mean random variables with the covariance matrix [23]:

$$\langle \vec{a}\vec{a}^T \rangle_{(ai)(bj)} \equiv \phi_{(ai)(bj)} = \delta_{ij} \left(\Gamma_{ab} \Phi_i + \delta_{ab} \varphi_{a,i} \right), \tag{3.6}$$

where i and j index the frequency bin and a and b refer to two pulsars. At this point, the ORF Γ_{ab} also enters the analysis together with the model-dependent coefficient Φ_i, which is related to Ω_{SGWB} by [23, 25]

$$\Omega_{\text{SGWB}} = \frac{8\pi^4 f^5}{H_0^2} \Phi(f) T_{\text{obs}}, \tag{3.7}$$

where $\Phi_i = \Phi(i/T_{\text{obs}})$. Pulsar-intrinsic red noise φ_a is modeled with a power law:

$$\varphi_a(f) = \frac{A_a^2}{12\pi^2} \frac{1}{T_{\text{obs}}} \left(\frac{f}{\text{year}^{-1}} \right)^{-\gamma_a} \text{year}^3, \tag{3.8}$$

where once again $\varphi_{a,i} = \varphi(i/T_{\text{obs}})$ [23]. $\boldsymbol{M}$ contains the partial derivatives of the TOAs with respect to each model parameter, evaluated at the initial best-fit values. $\vec{\epsilon}$ contains the offset to the fit parameter, so together they account for timing residuals due to deviations in timing models [23]. After marginalizing over every parameter that is not contained in Γ_{ab} or $\Phi(f)$ (we collect all parameters left in the array $\vec{\theta}$), we find the likelihood [23, 26, 27]

$$p(\vec{\delta t}|\vec{\theta}) = \frac{\exp\left(-\frac{1}{2} \vec{\delta t}^T \boldsymbol{C}^{-1} \vec{\delta t} \right)}{\sqrt{\det(2\pi \boldsymbol{C})}}, \tag{3.9}$$

with $\boldsymbol{C} = \langle \vec{n}\vec{n}^T \rangle + [\boldsymbol{M}, \boldsymbol{F}] \text{diag}(\infty, \boldsymbol{\phi}) [\boldsymbol{M}, \boldsymbol{F}]^T$ (∞ being a diagonal matrix with infinity as its entries, which means that $\vec{\epsilon}$ has flat priors). Rather than evaluating the full posterior distribution via direct integration, we employ a Markov Chain Monte Carlo (MCMC) algorithm to draw samples from it.

This is done iteratively, where we explore a multidimensional parameter space. Markov chains are stochastic processes that describe event sequences, and Monte Carlo algorithms are based on randomization. The most basic MCMC implementation is the Metropolis-Hastings algorithm. An initial vector $\vec{x}_0$ is taken from the prior. Now, the algorithm enters an iterative process that can theoretically run indefinitely. During the i iteration, a trial point $\vec{y}$ is drawn from the proposal distribution $q(\vec{y}, \vec{x}_{i-1})$. Then the Metropolis-Hastings ratio [9]

$$\mathrm{MH} = \frac{p(\vec{y})p(d|\vec{y})}{p(\vec{x}_{i-1})p(d|\vec{x}_{i-1})}\frac{q(\vec{x}_{i-1}|y)}{q(\vec{y}|\vec{x}_{i-1})} \tag{3.10}$$

is computed. For $\mathrm{MH} \geq 1$ the move in parameter space improved the model, therefore $\vec{x}_i = \vec{y}$ and the iteration continues with $i+1$. For $\mathrm{MH} < 1$, a random number u is drawn from a uniform distribution between 0 and 1. We can interpret MH as a success probability of the proposed parameter vector $\vec{y}$. For $u < \mathrm{MH}$ the step is once again accepted. However, in case of $u > \mathrm{MH}$, $\vec{x}_i$ is set to $\vec{x}_{i-1}$.

3.4 Results

By comparing equation (2.39) and equation (2.53), we find [3]

$$\Omega_{\mathrm{SGWB}} = \frac{4\pi^2 f^3}{3H_0^2} I. \tag{3.11}$$

The simplest ansatz for I is a power law

$$I(f) = \frac{A^2}{2f}\left(\frac{f}{f_{\mathrm{ref}}}\right)^{2\alpha}, \tag{3.12}$$

with $f_{\mathrm{ref}} = 1/\mathrm{year}$. Usually, the results of computations are given with the parameter $\gamma \equiv 3 - 2\alpha$ [1]. We will focus on the power law, so using equation (2.72), we find $n_I = 2 - \gamma$ and $\alpha_I = 0$.

The numerical analysis is performed using the wrapper `PTArcade` [23, 28]. It allows the user to enter a model file, that defines the overlap reduction function and the model for the spectrum. We chose to use the analysis method provided by `ENTERPRISE` [29] and used extensions from `ENTERPRISE_EXTENSIONS` [30]. The analysis is done using the NANOGrav 15-year dataset [31]. Within `PTArcade`, we can define how many red noise components we want to include. Each component i corresponds to an element of the Fourier basis i/T_{obs} where T_{obs} is the total observation time. The components are truncated at the 30th component for the intrinsic red noise of each pulsar, which is a value recommended by NANOGrav. The truncation at relatively low frequencies is justified by the fact that the SGWB spectrum is expected to be at the lower end of the observable frequencies. The same can be done for the GW components themselves, which are truncated at the 14th element. As mentioned in section 3.2, we use model selection to compare our physical model of anisotropies to an astrophysical interpretation with supermassive black hole binaries (SMBHB). The ratio of samples that are spent within each of the two models gives the Bayes factor. The GWB signal coming from the SMBHB is modeled as

$$h^2\Omega_{\text{GW}}(f) = \frac{2\pi^2 A_{\text{BHB}}^2}{3H_0^2}\left(\frac{f}{\text{year}^{-1}}\right)^{5-\gamma_{\text{BHB}}} \text{year}^{-2}, \tag{3.13}$$

where we give a limit to the amplitude A_{BHB} to $-18 < \log_{10}(A) < -11$ [23]. For more information on this, please refer to [32, 33]. The two most important model files, containing the exact and approximated autocorrelation (with and without fL_a-terms), can be found in appendix C.

First, we attempt to reproduce the results found in figure 2 of [3], where they find an upper limit of $\beta < 0.297$ at a $95\,\%$ credible level (CL) (constructed using the highest posterior density interval). In their analysis, they fixed the red noise parameters for each individual pulsar by taking the median values provided by the example analysis in [34], specifically with the data in `curn_14f_pl_vg.core`. The red noises of individual pulsars are modeled by equation (3.8). Normally, this is done by sampling the posterior distribution with a uniform prior with its boundaries at $-20 < \log_{10}(A_a) < -11$ and $0 < \gamma_a < 7$ for each parameter and pulsar individually. In order to fix the red noise parameter, a modified implementation of `PTArcade` was used. Using this, we fix the red noise parameter γ to their median values and a very narrow uniform prior for $\log_{10} A$. For each pulsar, $\log_{10} A$ is chosen to be within $\pm 10\,\%$ of the median value of the data recovered from `curn_14f_pl_vg.core`. We determined that the distinctive exponentially decaying β-posterior with its maximum at zero reported in [3] (as can be seen in figure 2 of their analysis) arises exclusively under the condition $\Gamma_{ab} = 1$, independent of the relative contributions from the linear and quadratic terms in β. In addition, this first analysis uses the expression for $\Gamma^{(2)}_{ab}$ presented in [3]. The result for $1.5 \cdot 10^5$ samples (sample sizes are calculated after the burn-in has been removed and the dataset thinned by a factor of $1/10$) for this model is presented in figure 3.3a, which allows us to set an upper bound for $\beta < 0.136$ at $95\,\%$ CL (the $95\,\%$ and $68\,\%$ CL are marked by dashed lines). Using model selection, we report a Bayes factor of $\mathcal{B} = 4.1 \pm 3.4$.

The red noise parameters were taken from available data sets, rather than being sampled. Increased computational power is provided by the PALMA-II HPC cluster, which runs multiple chains simultaneously. The results for sampling eight subchains with a total amount of 10^6 samples are shown in figure 3.3b. Sampling for all pulsars over the red noise parameter shows a much less constrained posterior for β. However, for now we still kept the autocorrelation to unity, leading to the exponentially decaying form of the posterior for β, achieving a much less constrained upper bound of $\beta < 0.77$ at $95\,\%$ CL. Unlike what is stated in [3], it cannot be observed that sampling over the red noise parameter leads to an insignificant deviation from the results presented in figure 3.3a. We have tested that longer computation times of up to two weeks do not significantly change the convergence on β.

Next, we will change the autocorrelation from unity to the analytical limit, taking $x_{ab} \to 0$. The resulting form of the autocorrelation can be found in equation (2.81) (10^6 samples). In addition, we use our own results for $\Gamma^{(2)}_{ab}$. The posteriors are seen in figure 3.4. Once again, we achieve a much less constrained upper bound with β at $\beta < 0.90$ at $95\,\%$ CL. Using the different autocorrelation significantly affected the posterior. Most of the posterior density for β is still located near zero.

Our final model uses the autocorrelation derived in equation (2.83), equation (2.86), and equation (2.87). Within the model file, the distance parameters are imported from the 15-year dataset. Their priors are modeled as truncated normal distributions ($0\,\mathrm{kpc}$ to $10\,\mathrm{kpc}$) restricted to physically meaningful, non-negative values. This truncation is necessary because the corresponding untruncated normal distributions, centered on the estimated mean pulsar distances, may assign significant probability to negative (and thus unphysical) values due to their large standard deviations. The results using 20 subchains with a total of $2.7 \cdot 10^6$ samples can be found in figure 3.5a. Interestingly, the posterior for β does not have a maximum

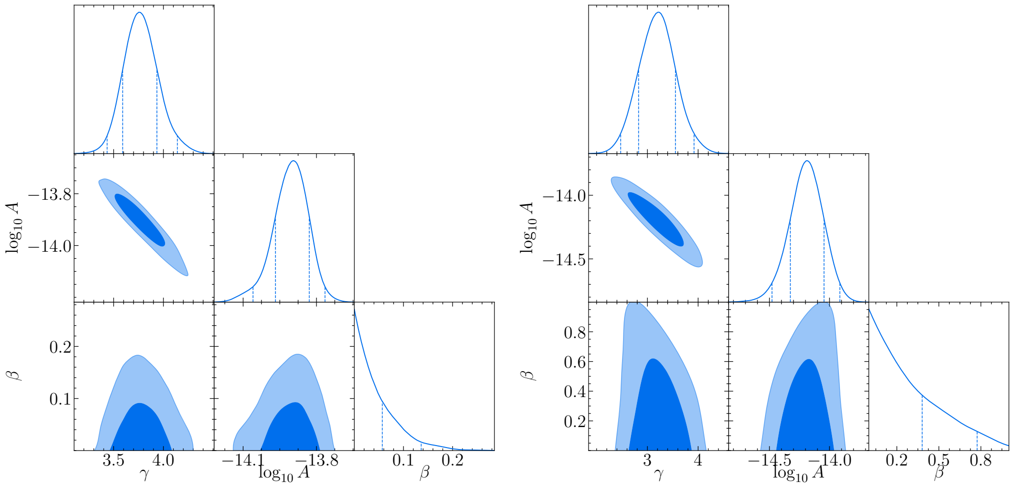

(a) (b)

Figure 3.3: Posteriors obtained by keeping the autocorrelation to unity and using the results for $\Gamma_{ab}^{(2)}$ from [14]. On the left are the results from a local run using the modified PTArcade version and fixing the red noise parameter. They represent the closest recreation of the results in [3]. We set an upper bound for $\beta < 0.136$ at $95\,\%$ CL. On the right are the results for the same model except for the fact that we sampled over red noise parameters and that the computations where performed on the cluster. We set an upper bound for $\beta < 0.77$ at $95\,\%$ CL.

near $\beta = 0$. The upper bound at $95\,\%$ CL for β is now 0.88. Looking at the plots of each individual subchain roughly containing $0.135 \cdot 10^6$ samples, reveals that the posterior shape for β varies (as can be seen in figure 3.5b and figure 3.5c). We have tested if constraining the pulsar distances further (limiting the upper and lower bound of the priors further) lead to different outcomes for the posterior shape, which it does not. Further consistency tests were also conducted, by either fixing fL_a to values withing the range $\mathcal{O}(100...10000)$ or assigning all pulsars to their collective mean distance, so that in both cases there is no need for sampling the pulsar distances. Though, one can still sample the pulsar distances and choose not to use them. Comparable results to those shown in figure 3.4 are obtained only when choosing not to sample pulsar distances, regardless of the test model used. This behavior and the fact that the subchains undergo significant shifts during sampling, suggest a computational artifact rather than a physical effect (see chapter 4 for a detailed discussion). Our results are summarized in table 3.1. Interestingly,

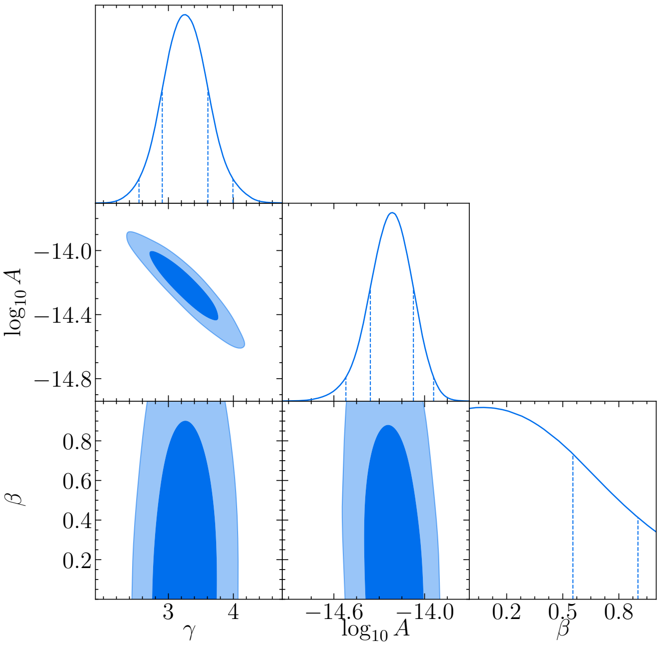

Figure 3.4: Posteriors obtained by using the limit $x_{ab} \to 0$ as the autocorrelation and applying our own results for $\Gamma_{ab}^{(2)}$ after 8.9×10^5 samples. We set an upper bound for β at $\beta < 0.90$ at $95\,\%$ CL. The maximum posterior value for $\beta = 0.068$ is reached.

the upper bounds for the later two models seem to largely agree (also for the $68\,\%$ CL as can be seen in figure 3.4 and figure 3.5a)

Figure	AC	RN sampling	$\Gamma_{ab}^{(2)}$	UB β	$\mathcal{B}$
3.3a	Unity	No	from [15]	0.136	4.1 ± 3.4
3.3b	Unity	Yes	from [15]	0.77	0.412 ± 0.022
3.4	Limit	Yes	our result	0.90	0.754 ± 0.038
3.5a	Exact	Yes	our result	0.88	1.287 ± 0.036

Table 3.1: Upper bounds (UB) at $95\,\%$ CL for β found for different analyses. We considered different possibilities for the autocorrelation (AC) and red noise (RN) sampling. The Bayes factor $\mathcal{B}$ is also given.

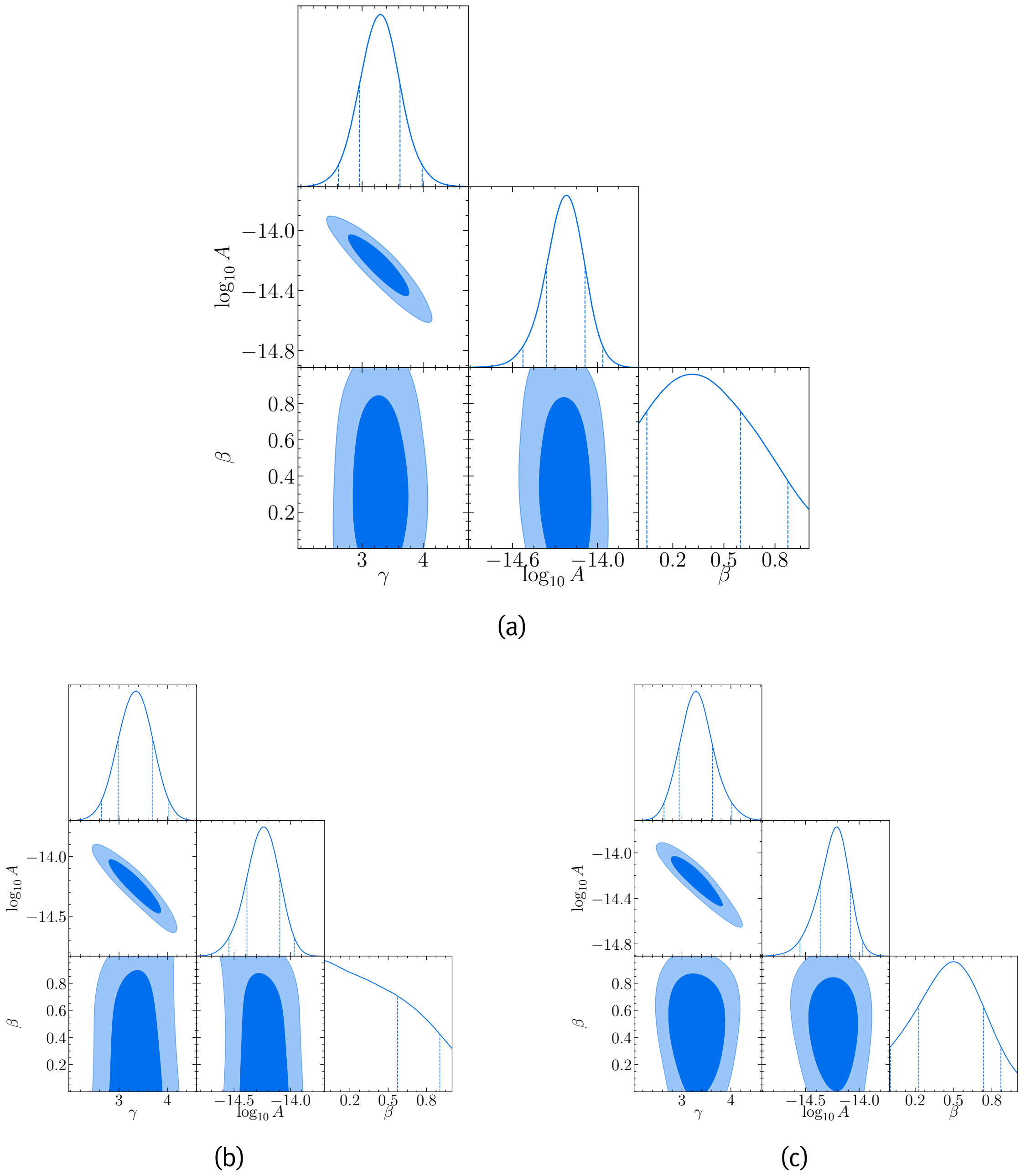

(a)

(b)

(c)

Figure 3.5: Posteriors obtained using the fL_a contributions within the autocorrelation and sampling over the red noise parameter using $2.7 \cdot 10^6$ samples. The form of the posterior (a) changes significantly revealing a maximum at $\beta = 0.31^{+0.28}_{-0.27}$ (upper and lower limit for $68\,\%$ of the posterior density). The Bayesian factor is $\mathcal{B} = 1.287 \pm 0.036$. The lower two plots ((b) & (c)) show two subchain plots from the run above.

Discussion

4

Anisotropies in the SGWB may originate not only from a kinematic effect. In fact, a significant contribution to the SGWB may arise from astrophysical sources such as SMBHBs. If the majority of the GWB is produced by SMBHB of masses $10^8 - 10^{10} M_\odot$, then anisotropies form because of the distribution and clustering of these astrophysical objects [35]. Anisotropy searches are usually performed using a product ansatz

$$I(f, \hat{\boldsymbol{n}}) = I(f) P(\hat{\boldsymbol{n}}) \tag{4.1}$$

(there are also frequency-resolved $P(\hat{\boldsymbol{n}}, f)$ anisotropy searches). A natural and widely adopted approach to model the angular dependence of the GWB power distribution $P(\hat{\boldsymbol{n}})$ is to expand it in terms of spherical harmonics

$$P(\hat{\boldsymbol{n}}) = \sum_{\ell=0}^{\infty} \sum_{m=-\ell}^{\ell} c_{\ell m} Y_\ell^m \tag{4.2}$$

with the coefficients

$$C_\ell = \frac{1}{2\ell + 1} \sum_{m=-\ell}^{\ell} |c_{\ell m}|^2 \tag{4.3}$$

and real-valued spherical harmonics Y_ℓ^m [36, 2]. In the case of an isotropic GWB, only the monopole term ($\ell = 0$) contributes to the angular power spectrum. Anisotropic characteristics manifest themselves as power in higher-order multipoles ($\ell > 0$). Theoretical modeling and numerical simulations of a GWB sourced by SMBHBs suggest that the anisotropic contributions remain subdominant, with $C_{\ell>0}/C_0 \lesssim 20\%$ [2, 35]. In the NANOGrav 15-year data set and the corresponding anisotropy search [2], no significant evidence for a power law or frequency-resolved anisotropy was found. They expect the sensitivity to scale with the number of monitored pulsars and observed time scale. Although their analysis was performed under the assumption of a SGWB of astrophysical origin, they specifically mention that the detection of a large-scale anisotropy could indicate the existence of an over-dense cluster of SMBHB *or* a kinematic effect [2], justifying our preceding analysis. Our analysis does not yield a statistically significant detection of dipole anisotropy, and we are only able to place upper limits on β. However, these constraints are less stringent than expected, as evidenced by our results.

A conservative estimate presented in [37] suggests that detecting a kinematic dipole in the gravitational wave background at the 90% confidence level would require $\mathcal{O}(10^2)$ frequency bins and approximately $\mathcal{O}(10^4)$ pulsars. The study also emphasizes the role of cosmic variance, a fundamental limitation in cosmological measurements arising from the fact that we observe only a single realization of the universe. This limitation necessitates the use of time-averaged statistics in place of ensemble averages. For PTA observations, cosmic variance can lead to variations in sensitivity to anisotropic signals of up to 15% at the 1σ level [37]. Notably, the dipole component of the anisotropy is relatively robust against cosmic variance, with sensitivity fluctuations limited to approximately 3% at 1σ [37].

An amplitude of GWB power spectrum spread in multipoles $\ell \geq 1$ is generally indicative of an astrophysical origin, particularly, one dominated by SMBHBs [38, 39]. In contrast, cosmological sources are expected to produce significantly weaker intrinsic anisotropies, with the dominant contribution, albeit still subdominant relative to astrophysical models, arising from the kinematic dipole $\ell = 1$ [3, 40]. In [40] they found that up to $49\,\%$ of realizations of an isotropic ensemble lead to a false detection of anisotropy due to interference of GW radiation from different directions, which changes the ORF. For future PTA anisotropies searches, they suggest updated null distributions for anisotropic backgrounds that incorporate possible interferences. Thus, our different approach for observing anisotropies within PTA data due to a kinematic dipole is still justified, since other searches without the updated null distribution presented in [40] have a high false positive detectability, relativizing previous findings that seem to be just at the brink of discovery.

Our analysis solely used a power law. Nonetheless, other well-motivated models of the intensity I, parameterized by spectral indices n_I and α_I, may also be considered. It was suspected, that some models can produce spectral tilt values for n_I

and α_I that potentially offset the suppression associated with the small value of β as indicated in equation (2.71) [15]. Models like these are, for example, discussed in [41]. Recently, it was discovered that for such models the Taylor expansion in β is not valid [42]. Still, at small spectral tilts, the sensitivity to kinematic anisotropies could be used to identify the spectral shape of the SGWB. This is done in [14] and in addition to that they deal with how intrinsic anisotropies are changed by a Doppler-boosted GWB (for the case that the spectral tilts do not compensate for β). They find that intrinsic anisotropies are mixed with those that come from kinematics, such that the observed dipole amplitude in our frame of reference can be a combination of the purely kinematic dipole contribution of the SGWB rest-frame monopole and a modulated contribution of the intrinsic quadrupole that appears for us as a dipole contribution even at linear order of β. Our model discussed above cannot distinguish between purely kinematic dipole and Doppler-shifted quadrupole contributions of the intrinsic anisotropy. Regarding sensitivity to spectral tilts, the findings in [14] demonstrate that, under a simplified model assuming a SMBHB origin, the spectral shape can be constrained with a precision of approximately $16\,\%$, while the measurement of the observer's velocity β can achieve a precision of $30\,\%$.

Placing upper limits on the dimensionless velocity parameter β, as done in our analysis and in [3], provides an independent method of constraining our peculiar velocity relative to the CMB rest frame (under the assumption that CMB and SGWB share a frame in which they appear isotropic). Although the kinematic dipole observed in the CMB is a well-established and extensively studied phenomenon, recent analyses have called into question the consistency of its inferred amplitude. In particular, discrepancies between the CMB dipole and the observed large-scale matter dipole, highlighted by the Ellis & Baldwin test (EBT), have raised concerns [43]. The idea behind the EBT is essentially to validate the claim of the ΛCDM model of our universe that the scale factor $a(t)$ of the universe's expansion is on large scales direction independent. By comparing the kinematic CMB dipole to the kinematic matter dipole of cosmological large-scale structures (for example, powerful radio galaxies and quasars), they found that while the direction of the dipole approximately agrees with that of the CMB, the magnitude is roughly two to three times larger (depending on the observed large-scale structure) [43]. An independent test of the kinematic dipole amplitude could provide valuable insight on the tension between matter and CMB dipole.

Our contribution to the topic is our reconsideration of the autocorrelation and expansion up to the second order of β largely inspired by the treatment in [5]. Since $fL_a \sim \mathcal{O}(100...1000)$ and enters at zeroth order of β as $(fL_a)^{-2}$, the resulting corrections are expected to be small. We observed that the maximum posterior estimate for β, as shown in figure 3.5a, shifted towards smaller values over the course of the sampling process. Multiple indications suggest that the deviation of the maximum posterior estimate from those obtained without including the fL_a terms is not physical, but rather the result of computational limitations. Specifically, the increased dimensionality that is introduced by sampling over pulsar distances. The correct autocorrelation only changes significantly for small values of fL_a. For some pulsars, these values are achievable, since their truncated prior has a non-negligible density for small distances. In additional tests, we found that the characteristic bell-shaped posterior for β with a maximum posterior value significantly deviating from zero seen in figure 3.5a emerged only when the pulsar distances were actively sampled. Importantly, the fixation of fL_a or just L_a had little effect on the posterior shape; instead, it was the act of sampling over pulsar distances that influenced the structure of the posterior (regardless of whether the sampled distances were used for calculations or not). Thus, we attribute the posterior shape observed in figure 3.5a to computational artifacts associated with the increased parameter space, rather than to physical effects. The increase of parameters is roughly $50\,\%$ (2×67 red noise parameter, 3 model parameter, 67 pulsar distances). This conclusion is also supported by the fact, that the posterior distributions for β found in the subchains have diverse shapes evolving differently during sampling and do not have a decisive form (see figure 3.5b and figure 3.5c). Nevertheless, the upper bounds on β remain broadly consistent with those obtained under red noise parameter sampling. The weaker upper limit is also problematic when considering the Taylor expansion for $\beta \ll 1$.

Conclusion

5

In this Bachelor thesis the theory behind the searches for kinematic anisotropies in PTA data was derived (based on the approach in [14, 15]) and applied to the NANOGrav 15-year data. We found a different result for the ORF $\Gamma_{ab}^{(2)}$, which appears in the second order of β. The result presented in this thesis for $\Gamma_{ab}^{(2)}$ does not vanish in a totally orthogonal system in which both pulsar position vectors and the velocity vector together make up a Cartesian system. Furthermore, we spend time to point out the importance of the considered autocorrelation which leads to two calculations that make up our main results. One of these results (i) simply considers the limit for two pulsars at the same position $x_{ab} \to 0$ and multiplying the factor of $1 + \delta_{ab}$. The other (ii) is found by deriving the exact autocorrelation of the ORF where the oscillating pulsar terms do not vanish under the integral. The second method is largely inspired by the treatment in [5].

We used a numerical Bayesian analysis to find an upper limit of β. While in the first case (i) the upper limit previously found is significantly increased to $\beta < 0.90$ at $95\,\%$ CL the other model (ii) has a non-zero maximum posterior value at $\beta = 0.31^{+0.28}_{-0.27}$ (upper and lower limit for $68\,\%$ CL) and an upper bound $\beta = 0.88$. We attribute the significant shift of the maximum posterior density estimate to a computational artifact. Both results significantly weaken the constrain previously found. Our results therefore mainly fall in line with the previous findings in [2] that do not find a significant detection for any anisotropy. However, it puts into question the Taylor expansion for β.

We noted the importance of searches for kinematic anisotropies as an independent confirmation of the kinematic anisotropies found in CMB data. This is made under the assumption that the rest-frame in which the SGWB appears isotropic is shared by the CMB. This is a reasonable assumption for a cosmological origin of the

SGWB. In fact, we assumed that the direction of the dipole is the same as found in CMB data and β of the smallness that a Taylor expansion can be truncated. Further studies could also use the framework developed in this thesis to search for an unfixed kinematic dipole, for example by freeing the directional parameters of $\hat{\boldsymbol{v}}$. As other studies have shown, the dipole is especially reliably detectable compared to other multipoles. Also, as was done in [5], one could combine kinematic anisotropy searches with modified gravity to test for physics beyond the standard model.

Computations Regarding the Overlap Reduction Function

A

Here we present the full calculation of the overlap reduction function [3]:

$$\Gamma_{ab}^{(0)} = \frac{3}{8\pi}\int d\hat{\boldsymbol{n}} \sum_{\lambda} D_a^{\lambda} D_b^{\lambda} \tag{A.1}$$

$$\Gamma_{ab}^{(1)} = \frac{3}{8\pi}\int d\hat{\boldsymbol{n}} \sum_{\lambda} D_a^{\lambda} D_b^{\lambda} (\hat{\boldsymbol{n}}\hat{\boldsymbol{v}}) \tag{A.2}$$

$$\Gamma_{ab}^{(2)} = \frac{3}{8\pi}\int d\hat{\boldsymbol{n}} \sum_{\lambda} D_a^{\lambda} D_b^{\lambda} \left((\hat{\boldsymbol{n}}\hat{\boldsymbol{v}})^2 - \frac{1}{3} \right) \tag{A.3}$$

A.1 Monopole Contribution

In this section, we will look at the analytical solution of the Hellings-Downs curve, following the derivation in [20]. The integral becomes:

$$\Gamma_{ab}^{(0)} = \frac{3}{8\pi}\int d^2\hat{\boldsymbol{n}} \sum_{\lambda} D_a^{\lambda} D_b^{\lambda}. \tag{A.4}$$

The pulsar a will be fixed along the z-axis $\hat{x}_a = \hat{z}$ and pulsar b is located within the xz-plane, where we identify the angle between the pulsars as ξ:

$$\hat{\boldsymbol{n}}\hat{\boldsymbol{x}}_a = \cos\theta \tag{A.5}$$

$$\hat{\boldsymbol{n}}\hat{\boldsymbol{x}}_b = \cos\xi\cos\theta + \sin\xi\sin\theta\cos\phi. \tag{A.6}$$

Recall that the polarization tensors $\mathbf{e}_{ij}^{\lambda}(\hat{n})$ can be written in the following way:

$$e_{ij}^{+}(\hat{n}) = \hat{\theta}_i\hat{\theta}_j - \hat{\phi}_i\hat{\phi}_j \tag{A.7}$$

$$e_{ij}^{\times}(\hat{n}) = \hat{\theta}_i\hat{\phi}_j + \hat{\phi}_i\hat{\theta}_j, \tag{A.8}$$

where $\hat{\phi}$ and $\hat{\theta}$ denote the unit vectors of the spherical coordinates. In this coordinate system $\hat{n} = \hat{r}$. In order to evaluate the sum over λ, we calculate the products of the pulsar vectors and the polarization tensors:

$$\hat{x}_a^i \hat{x}_a^j e_{ij}^{+}(\hat{\boldsymbol{n}}) = \sin^2\theta \tag{A.9}$$

$$\hat{x}_a^i \hat{x}_a^j e_{ij}^{\times}(\hat{n}) = 0 \tag{A.10}$$

$$\hat{x}_b^i \hat{x}_b^j e_{ij}^{+}(\hat{n}) = (\sin\xi\cos\theta\cos\phi - \cos\xi\sin\theta)^2 - \sin^2\xi\sin^2\phi \tag{A.11}$$

$$\hat{x}_b^i \hat{x}_b^j e_{ij}^{\times}(\hat{\boldsymbol{n}}) = 2\,(\sin\xi\cos\theta\cos\phi - \cos\xi\sin\theta)\sin\xi\sin\phi. \tag{A.12}$$

It becomes clear that we can omit the ×-polarization in this coordinate system. It follows:

$$D_a^{+}(\hat{n}) = \frac{1}{2}\,(1-\cos\theta) \tag{A.13}$$

$$D_b^{+}(\hat{n}) = \frac{1}{2}\left[(1-\cos\xi\cos\theta-\sin\xi\sin\theta\cos\phi) - \frac{2\sin^2\xi\sin^2\phi}{1+\cos\xi\cos\theta+\sin\xi\sin\theta\cos\phi}\right] \tag{A.14}$$

and

$$\sum_{\lambda} D_a^{\lambda} D_b^{\lambda} = \frac{1}{2}\,(1-\cos\theta)$$
$$\frac{1}{2}\left[(1-\cos\xi\cos\theta-\sin\xi\sin\theta\cos\phi) - \frac{2\sin^2\xi\sin^2\phi}{1+\cos\xi\cos\theta+\sin\xi\sin\theta\cos\phi}\right]. \tag{A.15}$$

All of the ϕ-dependence is collected within the integral $I(x,\xi)$, where we used substitution to set $x = \cos\theta$ under the integral, leaving us with

$$\Gamma_{ab}^{(0)} = \frac{3}{16\pi}\int_{-1}^{1} dx\,(1-x)I(x,\xi) \tag{A.16}$$

to carry out. In order to solve $I(x,\xi)$, we split it into two parts, of which one, I_1, is trivially solved, and I_2 can be solved using contour integration.

$$\begin{aligned} I(x,\xi) \equiv \int_0^{2\pi} d\phi\ & \overbrace{\frac{1}{2}(1 - x\cos\xi - \sqrt{1-x^2}\sin\xi\cos\phi)}^{I_1(x,\xi)} \\ & - \underbrace{\frac{\sin^2\xi\sin^2\phi}{1 + x\cos\xi + \sqrt{1-x^2}\sin\xi\cos\phi}}_{I_2(x,\xi)}, \end{aligned} \tag{A.17}$$

$$I_1(x,\xi) \equiv \frac{1}{2}\int_0^{2\pi} d\phi\,(1 - x\cos\xi - \sqrt{1-x^2}\sin\xi\cos\phi = \pi(1 - x\cos\phi), \tag{A.18}$$

$$\begin{aligned} I_2(x,\xi) &\equiv -\sin^2\xi \int_0^{2\pi} d\phi\, \frac{\sin^2\phi}{1 + x\cos\xi + \sqrt{1-x^2}\sin\xi\cos\phi} \\ &= -\sin^2\xi \oint_C dz\, f(z) \end{aligned} \tag{A.19}$$

In the last equivalence symbol we apply the substitution $z = \exp(i\phi)$. This leaves us with the following:

$$f(z) = \frac{i(z^2-1)^2}{z^2\left[4z(1 + x\cos\xi) + 2\sqrt{1-x^2}\sin\xi(z^2+1)\right]}. \tag{A.20}$$

The part of the denominator of $f(z)$ that is enclosed in square brackets can be written in terms of its poles. This can be done by factoring out $2\sqrt{1-x^2}\sin\xi$ and applying the quadratic equation in terms of z:

$$4z(1 + x\cos\xi) + 2\sqrt{1-x^2}\sin\xi(z^2+1) = 2\sqrt{1-x^2}\sin\xi(z - z_+)(z - z_+). \tag{A.21}$$

When applying the quadratic formula, the term $|\cos\xi + x|$ arises; therefore, we divide the integral over x into two parts for two regions. In the following, the integral from $-\cos\xi \leq x \leq 1$ will refer to the top sign and $-1 \leq x \leq -\cos\xi$ to the bottom one:

$$z_+ \equiv -\sqrt{\left(\frac{1 \mp \cos\xi}{1 \pm \cos\xi}\right)\left(\frac{1 \mp x}{1 \pm x}\right)} \qquad\qquad z_- \equiv \frac{1}{z_+} \tag{A.22}$$

To see which of these poles is within the unit circle to calculate the residue, we look at their absolute value and estimate from there:

$$|z_+| = \left|\sqrt{\left(\frac{1 \mp \cos\xi}{1 \pm \cos\xi}\right)\left(\frac{1 \mp x}{1 \pm x}\right)}\right| \leq \left|\sqrt{\left(\frac{1 \mp \cos\xi}{1 \pm \cos\xi}\right)\left(\frac{1 \pm \cos\theta}{1 \mp \cos\theta}\right)}\right| \leq 1. \tag{A.23}$$

Thus, z_+ is within the unit circle, and it follows that $|z_-| = 1/|z_+|$ cannot be within the unit circle too. To summarize, until this point we have found two poles of $f(z)$, namely z_+ and 0 the latter of which is a pole of order two. The definition of a residue of order n at z_0 is the following:

$$\mathrm{Res}(f(z), z_0) = \lim_{z \to z_0} \frac{1}{(n-1)!} \frac{d^{n-1}}{dz^{n-1}} (f(z)(z - z_0)^n), \tag{A.24}$$

leaving us with

$$\mathrm{Res}(f(z), z_+) = \frac{i(z_+ - z_-)}{2\sqrt{1 - x^2}\sin\xi} \tag{A.25}$$

$$\mathrm{Res}(f(z), 0) = \frac{i(z_+ + z_-)}{2\sqrt{1 - x^2}\sin\xi}. \tag{A.26}$$

Applying the residue theorem gives the result for I_2

$$\oint_C f(z)dz = 2\pi i \sum_i \mathrm{Res}(f, z_i) = \frac{2\pi}{(1 \pm x)(1 \pm \cos\xi)}, \tag{A.27}$$

and putting everything together;

$$I(x, \xi) = \pi(1 - x\cos\xi) - 2\pi \frac{1 \mp \cos\xi}{1 \pm x}. \tag{A.28}$$

In the last step, we carry out the integration over x where we consider our defined regions, therefore our integral splits into three parts:

$$\begin{aligned}\Gamma_{ab}^{(0)} &= \frac{3}{16}\left[\int_{-1}^{1} dx\,(1-x)(1-x\cos\xi)\right] \\ &- \frac{6}{16}\left[(1+\cos\xi)\int_{-1}^{-\cos\xi} dx\right] - \frac{6}{16}\left[(1-\cos\xi)\int_{-\cos\xi}^{1} dx\,\frac{1-x}{1+x}\right] \\ &= \frac{1}{2} - \frac{1}{4}\left(\frac{1-\cos\xi}{2}\right) + \frac{3}{2}\left(\frac{1-\cos\xi}{2}\right)\ln\left(\frac{1-\cos\xi}{2}\right) \\ &= \frac{1}{2} - \frac{1}{4}x_{ab} + \frac{3}{2}x_{ab}\ln\left(x_{ab}\right),\end{aligned} \tag{A.29}$$

with

$$x_{ab} \equiv \frac{1-\cos\xi}{2} \equiv \frac{1-\hat{\boldsymbol{x}}_a\hat{\boldsymbol{x}}_b}{2}. \tag{A.30}$$

A.2 Dipole Contribution

The dipole moment enters the integral with a factor of $\hat{\boldsymbol{n}}\hat{\boldsymbol{v}}$, where $\hat{\boldsymbol{v}}$ is the unit vector of the velocity of our Barycenter's moving reference frame (however, in theory it can be any vector for the computation). The derivation follows the example in [44] but uses methods similar to those used in the previous section.

The relevant integral looks like this:

$$\Gamma_{ab}^{(1)} = \frac{3}{8\pi}\int d^2\hat{\boldsymbol{n}}\,(\hat{\boldsymbol{n}}\hat{\boldsymbol{v}})\sum_{\lambda} D_a^{\lambda} D_b^{\lambda}, \tag{A.31}$$

where we need to define the general direction of $\hat{\boldsymbol{v}}$ as

$$\hat{\boldsymbol{v}} \equiv (\sin\alpha_1\cos\eta, \sin\alpha_1\sin\eta, \cos\alpha_1). \tag{A.32}$$

Thus,

$$\hat{\boldsymbol{n}}\hat{\boldsymbol{v}} = \cos\alpha_1\cos\theta + \sin\alpha_1\sin\theta\cos(\phi-\eta) \tag{A.33}$$

$$\hat{\boldsymbol{v}}\hat{\boldsymbol{x}}_a = \cos\alpha_1 \tag{A.34}$$

$$\hat{\boldsymbol{v}}\hat{\boldsymbol{x}}_b = \cos\alpha_1\cos\xi + \sin\alpha_1\sin\xi\cos\eta \equiv \cos\alpha_2. \tag{A.35}$$

Plugging everything into the integral, we receive the following:

$$\Gamma^{(1)}_{ab} = \frac{3}{16\pi}\int d^2\hat{\boldsymbol{n}}\;[\cos\alpha_1\cos\theta + \sin\alpha_1\sin\theta(\cos\eta\cos\phi + \sin\phi\sin\eta)]$$
$$\frac{1}{2}(1-\cos\theta)\left[(1-\cos\xi\cos\theta - \sin\xi\sin\theta\cos\phi) - \frac{2\sin^2\xi\sin^2\phi}{1+\cos\xi\cos\theta+\sin\xi\sin\theta\cos\phi}\right], \tag{A.36}$$

we once again make the substitution $x = \cos\theta$ where we observe that the integral can be split into three parts. Each part is defined by the prefactor within the first square brackets:

$$\Gamma^{(1)}_{ab} = \frac{3}{16\pi}\int_{-1}^{1} dx\,(1-x)$$
$$\left[\cos\alpha_1 x J_1(x,\xi) + \sin\alpha_1\sqrt{1-x^2}\cos\eta J_2(x,\xi) + \sin\alpha_1\sqrt{1-x^2}\sin\eta J_3(x,\xi)\right] \tag{A.37}$$

Now we evaluate every integral over ϕ separately. J_1 is the same as I in equation (A.28)

$$J_1 \equiv \pi(1 - x\cos\xi) - 2\pi\frac{1\mp\cos\xi}{1\pm x}, \tag{A.38}$$

while J_2 and J_3 are the same integral modified with a factor of $\cos\phi$ and $\sin\phi$, respectively. Each of these integrals can be further split apart following the example in the previous section ($J_2 \equiv J_{2.1} + J_{2.2}$, $J_3 \equiv J_{3.1} + J_{3.2}$):

$$J_{2.1} \equiv \frac{1}{2}\int_0^{2\pi} d\phi\;\cos\phi(1 - x\cos\xi - \sqrt{1-x^2}\sin\xi\cos\phi) = -\frac{\pi}{2}\sqrt{1-x^2}\sin\xi \tag{A.39}$$

$$J_{3.1} \equiv \frac{1}{2}\int_0^{2\pi} d\phi\;\sin\phi(1 - x\cos\xi - \sqrt{1-x^2}\sin\xi\cos\phi) = 0 \tag{A.40}$$

$$J_{2.2} \equiv -\sin^2\xi\int_0^{2\pi} d\phi\,\frac{\sin^2\phi\cos\phi}{1 + x\cos\xi + \sqrt{1-x^2}\sin\xi\cos\phi} \tag{A.41}$$

$$J_{3.2} \equiv -\sin^2\xi\int_0^{2\pi} d\phi\,\frac{\sin^3\phi}{1 + x\cos\xi + \sqrt{1-x^2}\sin\xi\cos\phi}. \tag{A.42}$$

To deal with the second part of both integrals, we once again make use of the substitution $z = \exp(i\phi)$ similar to the non-dipol integral and use the same definitions as in equation (A.22)

$$J_{2.2} = -\frac{\sin^2\xi}{2}\oint_C dz\, \underbrace{\frac{i(z^2-1)^2(z^2+1)}{2\sqrt{1-x^2}\sin\xi z^3(z-z_+)(z-z_-)}}_{f_{2.2}(z)} \tag{A.43}$$

$$J_{3.2} = -\frac{\sin^2\xi}{2}\oint_C dz\, \underbrace{\frac{(z^2-1)^3}{2\sqrt{1-x^2}\sin\xi z^3(z-z_+)(z-z_-)}}_{f_{3.2}(z)}, \tag{A.44}$$

observing that the residue at pole $z_0 = 0$ is now of order three

$$\mathrm{Res}(f_{2.2}(z),0) = \frac{i(z_+^2+z_-^2)}{2\sqrt{1-x^2}\sin\xi} \tag{A.45}$$

$$\mathrm{Res}(f_{3.2}(z),0) = -\frac{(z_+-z_-)^2}{2\sqrt{1-x^2}\sin\xi} \tag{A.46}$$

$$\mathrm{Res}(f_{2.2}(z),z_+) = \frac{i(z_+^2-z_-^2)}{2\sqrt{1-x^2}\sin\xi} \tag{A.47}$$

$$\mathrm{Res}(f_{3.2}(z),z_+) = \frac{(z_+-z_-)^2}{2\sqrt{1-x^2}\sin\xi}, \tag{A.48}$$

and thus

$$J_{2.2} = -\frac{\sin^2\xi}{2}2\pi i\sum_i \mathrm{Res}(f_{2.2}(z),z_i) = z_+^2\frac{\pi\sin\xi}{\sqrt{1-x^2}} \tag{A.49}$$

$$J_{3.2} = -\frac{\sin^2\xi}{2}2\pi i\sum_i \mathrm{Res}(f_{3.2}(z),z_i) = 0, \tag{A.50}$$

resulting in

$$J_2 = -\frac{\pi}{2}\sqrt{1-x^2}\sin\xi + \left(\frac{1\mp\cos\xi}{1\pm\cos\xi}\right)\left(\frac{1\mp x}{1\pm x}\right)\frac{\pi\sin\xi}{\sqrt{1-x^2}} \tag{A.51}$$

$$J_3 = 0. \tag{A.52}$$

Finally, we can put everything together and once again integrate over x where we respect the established regions of $[-1; -\cos\xi]$ and $[-\cos\xi; 1]$:

$$
\begin{aligned}
\Gamma^{(1)}_{ab} &= \frac{3}{16}\Bigg\{ \int_{-1}^{1} dx\,(1-x)\Bigg[\cos\alpha_1 x \left((1 - x\cos\xi) - 2\frac{1\mp\cos\xi}{1\pm x} \right) \\
&+ \sin\alpha_1 \sqrt{1-x^2}\cos\eta \Bigg(-\frac{1}{2}\sqrt{1-x^2}\sin\xi \\
&+ \left(\frac{1\mp\cos\xi}{1\pm\cos\xi}\right)\left(\frac{1\mp x}{1\pm x}\right)\frac{\sin\xi}{\sqrt{1-x^2}} \Bigg)\Bigg]\Bigg\} \\
&= \frac{3}{16}\Bigg\{ \int_{-1}^{1} dx\,(1-x)\cos\alpha_1 x(1-x\cos\xi) \\
&- 2\int_{-1}^{-\cos\xi} dx\ \cos\alpha_1 x(1+\cos\xi) - 2\int_{-\cos\xi}^{1} dx\ \cos\alpha_1 x(1-\cos\xi)\frac{1-x}{1+x} \\
&+ \sin\alpha_1\cos\eta\sin\xi\Bigg[-\frac{1}{2}\int_{-1}^{1} dx\,(1-x)(1-x^2) \\
&+ \int_{-1}^{-\cos\xi} dx\ \left(\frac{1+\cos\xi}{1-\cos\xi}\right)(1+x) + \int_{-\cos\xi}^{1} dx\ \left(\frac{1-\cos\xi}{1+\cos\xi}\right)\frac{(1-x)^2}{1+x}\Bigg]\Bigg\} \\
&= \frac{3}{16}\Bigg\{ -\frac{2}{3} - \cos\alpha_1(\cos\xi+1)(\cos^2\xi-1) + \\
&\cos\alpha_1\left(-4(1-\cos\xi)\ln\left(\frac{1-\cos\xi}{2}\right) - (1-\cos\xi)(1+\cos\xi)(\cos\xi+3)\right) \\
&\sin\alpha_1\cos\eta\sin\xi\Bigg[-\frac{2}{3} - 2(1-\cos\xi) - 4\frac{1-\cos\xi}{1+\cos\xi}\ln\left(\frac{1-\cos\xi}{2}\right)\Bigg]\Bigg\} \\
&= \frac{3}{16}\Bigg\{ (\cos\alpha_1(\cos\xi+1) + \sin\alpha_1\cos\eta\sin\xi) \\
&\left(-\frac{2}{3} - 2(1-\cos\xi) - 4\frac{1-\cos\xi}{1+\cos\xi}\ln\left(\frac{1-\cos\xi}{2}\right)\right)\Bigg\} \\
&= [\cos\alpha_1 + \cos\alpha_2]\left(-\frac{1}{8} - \frac{3}{4}x_{ab} - \frac{3x_{ab}\ln x_{ab}}{4\,(1-x_{ab})}\right) \\
&= [\hat{\boldsymbol{v}}\hat{\boldsymbol{x}}_a + \hat{\boldsymbol{v}}\hat{\boldsymbol{x}}_b]\left(-\frac{1}{8} - \frac{3}{4}x_{ab} - \frac{3x_{ab}\ln x_{ab}}{4\,(1-x_{ab})}\right),
\end{aligned}
\tag{A.53}
$$

where in the second to last step, we applied equation (A.35).

A.3 Quadrupole Contributions

We solve the following integral:

$$\Gamma_{ab}^{(2)} = \frac{3}{8\pi}\int d^2\hat{\boldsymbol{n}}\,\left[(\hat{\boldsymbol{n}}\hat{\boldsymbol{v}})^2 - \frac{1}{3}\right]\sum_{\lambda} D_a^{\lambda} D_b^{\lambda}, \tag{A.54}$$

using the same definitions as in equation (A.33), one arrives at

$$\begin{aligned}
\Gamma_{ab}^{(2)} &= \frac{3}{16\pi}\int d^2\hat{\boldsymbol{n}}\Big[\cos^2\alpha_1\cos^2\theta + \sin^2\alpha_1\sin^2\theta\,[\cos\phi\cos\eta + \sin\phi\sin\eta]^2 \\
&\quad + 2\cos\alpha_1\sin\alpha_1\sin\theta\cos\theta[\cos\phi\cos\eta + \sin\phi\sin\eta] - \frac{1}{3}\Big]\frac{1}{2}(1-\cos\theta) \\
&\quad \left[(1-\cos\xi\cos\theta - \sin\xi\sin\theta\cos\phi) - \frac{2\sin^2\xi\sin^2\phi}{1+\cos\xi\cos\theta+\sin\xi\sin\theta\cos\phi}\right] \\
&= \frac{3}{16\pi}\int_{-1}^{1} dx\,(1-x)\Big\{\left[\cos^2\alpha_1 x^2 + \sin^2\alpha_1\cos^2\eta(1-x^2) - \frac{1}{3}\right] I(x,\xi) \\
&\quad + \sin^2\alpha_1(1-x^2)\left[(\sin^2\eta - \cos^2\eta)K(x,\xi) + 2\cos\eta\sin\eta\tilde{K}(x,\xi)\right] \\
&\quad + 2\cos\alpha_1\sin\alpha_1 x\sqrt{1-x^2}\,[\cos\eta J_2(x,\xi) + \sin\eta J_3(x,\xi)]\Big\}.
\end{aligned} \tag{A.55}$$

Where after the second equal sign, we replaced the integration over $d\cos\theta$ with dx and collected all ϕ-dependencies in $I(x,\xi)$, $J_{2/3}(x,\xi)$, $K(x,\xi)$ and $\tilde{K}(x,\xi)$. Once again $I(x,\xi)$ is equation (A.28), while $J_2(x,\xi)$ and $J_3(x,\xi)$ are found in equation (A.51) and equation (A.52). Also note that $\tilde{K}(x,\xi)$ is zero due to the integration over a period of an even and uneven function. We split $K(x,\xi) = K_1(x,\xi) + K_2(x,\xi)$ and perform similar integrations as above:

$$K_1 = \int_0^{2\pi} d\phi\,\frac{1}{2}\sin^2\phi\left(1 - x\cos\xi - \sqrt{1-x^2}\sin\xi\cos\phi\right) = \frac{\pi}{2}(1-x\cos\xi) \tag{A.56}$$

$$K_2 = -\sin^2\xi\int_0^{2\pi} d\phi\,\frac{\sin^4\phi}{1+x\cos\xi+\sin\xi\sqrt{1-x^2}\cos\phi}. \tag{A.57}$$

For K_2, the evaluation of the contour integral is

$$f(z) = \frac{1}{4i}\frac{(z^2-1)}{2\sqrt{1-x^2}\sin\xi\,(z-z_+)\,(z-z_-)\,z^4}, \tag{A.58}$$

with the residues

$$\operatorname{Res}(f(z),0) = \frac{1}{8i}\frac{z_+^3 - 3z_+ - 3z_- + z_-^3}{\sqrt{1-x^2}\sin\xi} \tag{A.59}$$

$$\operatorname{Res}(f(z),z_+) = \frac{1}{8i}\frac{(z_+ - z_-)^3}{\sqrt{1-x^2}\sin\xi} \tag{A.60}$$

such that $K(x,\xi)$ evaluates to

$$\begin{aligned} K(x,\xi) = {} & \frac{\pi}{2}(1 - x\cos\xi) + \\ & \frac{\pi\sin\xi}{2\sqrt{1-x^2}}\sqrt{\left(\frac{1\mp\cos\xi}{1\pm\cos\xi}\right)\left(\frac{1\mp x}{1\pm x}\right)}\left[\left(\frac{1\mp\cos\xi}{1\pm\cos\xi}\right)\left(\frac{1\mp x}{1\pm x}\right) - 3\right]. \end{aligned} \tag{A.61}$$

Our integral must still be evaluated over x, where we respect the dedicated regions and drag the respective terms with x dependencies into the integral

$$\begin{aligned} & \frac{3}{16}\int_{-1}^{1} dx\, \left[x^2\cos^2\alpha_1 + (1-x^2)\sin^2\alpha_1\cos^2\eta - \frac{1}{3}\right]\left(1 - x\cos\xi - 2\frac{1\mp\cos\xi}{1\pm x}\right)(1-x) \\ & + \sin^2\alpha_1\left[\sin^2\eta - \cos^2\eta\right]\Bigg(\frac{1}{2}(1-x\cos\xi)(1-x)(1-x^2) + \frac{1}{2}(1\mp\cos\xi)(1-x)(1\mp x) \\ & \left[\left(\frac{1\mp\cos\xi}{1\pm\cos\xi}\right)\left(\frac{1\mp x}{1\pm x}\right) - 3\right]\Bigg) \\ & + 2\sin\alpha_1\cos\alpha_1\sin\xi\cos\eta\left(-\frac{1}{2}x(1-x^2)(1-x) + \left(\frac{1\mp\cos\xi}{1\pm\cos\xi}\right)\left(\frac{1\mp x}{1\pm x}\right)x(1-x)\right) \\ & = \frac{3}{16}\Bigg\{\left(8x_{ab}\ln x_{ab} - \frac{2}{3}\cos^2\xi - 2\cos^2\xi + \frac{64}{60}\cos\xi + \frac{8}{3}\right)\cos^2\alpha_1 \\ & \left(-\frac{2}{3} - \frac{2}{5}\cos\xi + 2\cos^2\xi + \frac{2}{3}\cos^3\xi\right)\sin^2\alpha_1\cos^2\eta \\ & - \left(8x_{ab}\ln x_{ab} + \frac{2}{3}\cos\xi + 2\right)\frac{1}{3} \\ & + \sin^2\alpha_1\left[\sin^2\eta - \cos^2\eta\right]\Bigg\{\left(\frac{2}{15}\cos\xi + \frac{2}{3}\right) \\ & + \frac{4}{\cos\xi + 1}\left(-(1-\cos\xi)^2\ln x_{ab} + \cos^2\xi - 1\right)\Bigg\} \\ & + 2\sin\alpha_1\cos\alpha_1\sin\xi\cos\eta\left(\frac{2}{15} + \frac{2}{3(1+\cos\xi)}\left(12x_{ab}\ln x_{ab} + \sin^2\xi\cos\xi + 3\sin^2\xi\right)\right)\Bigg\}. \end{aligned} \tag{A.62}$$

Using the definitions for $\hat{\boldsymbol{v}}\hat{\boldsymbol{x}}_a$ and $\hat{\boldsymbol{v}}\hat{\boldsymbol{x}}_b$, we finally get:

$$\begin{aligned}\Gamma^{(2)}_{ab} = \frac{1}{(x_{ab}-1)^2}\Bigg\{ &\left(\frac{1}{4}x^3_{ab} - x^2_{ab} + \frac{3}{4}x_{ab}\ln x_{ab} + \frac{1}{2}x_{ab} + \frac{1}{4}\right)\left[(\hat{\boldsymbol{v}}\hat{\boldsymbol{x}}_a)^2 + (\hat{\boldsymbol{v}}\hat{\boldsymbol{x}}_b)^2\right] \\ &+ \left(\frac{3}{2}x^2_{ab}\ln x_{ab} - \frac{39}{20}x^2_{ab} + \frac{12}{5}x_{ab} - \frac{9}{20}\right)\left[(\hat{\boldsymbol{v}}\hat{\boldsymbol{x}}_a)(\hat{\boldsymbol{v}}\hat{\boldsymbol{x}}_b)\right] \\ + &\left(x^3_{ab}\ln x_{ab} - \frac{22}{15}x^3_{ab} - \frac{1}{2}x^2_{ab}\ln x_{ab} + \frac{35}{12}x^2_{ab} - \frac{1}{2}x_{ab}\ln x_{ab} - \frac{43}{30}x_{ab} - \frac{1}{60}\right)\Bigg\}. \end{aligned} \tag{A.63}$$

Taylor Expansion of the Anisotropic Intensity

B

Following the example in [15, 3], which expands on the ideas presented in [14], the intensity $I(f, \hat{\boldsymbol{n}})$ is Taylor expanded up to the order $\mathcal{O}(\beta^2)$. Recall that anisotropy comes into existence because of a Doppler shift that induces a $\hat{\boldsymbol{n}}$-dependent red shift onto the frequency:

$$\mathcal{D} = \frac{\sqrt{1-\beta^2}}{1-\beta\hat{\boldsymbol{n}}\hat{\boldsymbol{v}}} \tag{B.1}$$

$$f \to f' = \mathcal{D}^{-1} f. \tag{B.2}$$

If the $\hat{\boldsymbol{n}}$-dependency of the intensity can be fully explained through the above relation and using the fact that the energy density transforms like

$$\Omega_{\mathrm{SGWB}}(f) \to \mathcal{D}^4 \Omega_{\mathrm{SGWB}}(\mathcal{D}^{-1} f), \tag{B.3}$$

we can write

$$\frac{I(f, \hat{\boldsymbol{n}})}{\bar{I}(f)} = \mathcal{D}\frac{\bar{I}(\mathcal{D}^{-1}f)}{\bar{I}(f)}, \tag{B.4}$$

and expand it in orders of β

$$\begin{aligned} \mathcal{D}\frac{\bar{I}(\mathcal{D}^{-1}f)}{\bar{I}(f)} = 1 &+ \beta\left[\left(\frac{d\mathcal{D}}{d\beta}\right)\left(\frac{\bar{I}(\mathcal{D}^{-1}f)}{\bar{I}(f)}\right) + \mathcal{D}\left(\frac{d(\mathcal{D}^{-1}f)}{d\beta}\right)\left(\frac{d\bar{I}(\mathcal{D}^{-1}f)}{d(\mathcal{D}^{-1}f)}\right)\frac{1}{\bar{I}(f)}\right]_{\beta=0} \\ &+ \frac{\beta^2}{2}\left[\left(\frac{d^2\mathcal{D}}{d\beta^2}\right)\left(\frac{\bar{I}(\mathcal{D}^{-1}f)}{\bar{I}(f)}\right) + 2\left(\frac{d\mathcal{D}}{d\beta}\right)\left(\frac{d(\mathcal{D}^{-1}f)}{d\beta}\right)\left(\frac{d\bar{I}(\mathcal{D}^{-1}f)}{d(\mathcal{D}^{-1}f)}\right)\frac{1}{\bar{I}(f)}\right. \\ &\left. + \mathcal{D}\left(\frac{d^2(\mathcal{D}^{-1}f)}{d\beta^2}\right)\left(\frac{d\bar{I}(\mathcal{D}^{-1}f)}{d(\mathcal{D}^{-1}f)}\right)\frac{1}{\bar{I}(f)} + \mathcal{D}\left(\frac{d(\mathcal{D}^{-1}f)}{d\beta}\right)^2 \frac{d^2\bar{I}(\mathcal{D}^{-1}f)}{d(\mathcal{D}^{-1}f)^2}\frac{1}{\bar{I}(f)}\right]_{\beta=0}. \end{aligned} \tag{B.5}$$

We individually evaluate every differential such that

$$\left.\frac{dD}{d\beta}\right|_{\beta=0} = \hat{\boldsymbol{n}}\hat{\boldsymbol{v}} \tag{B.6}$$

$$\left.\frac{d^2 D}{d\beta^2}\right|_{\beta=0} = 2\left(\hat{\boldsymbol{n}}\hat{\boldsymbol{v}}\right)^2 - 1 \tag{B.7}$$

$$\left.\frac{d\mathcal{D}^{-1}}{d\beta}\right|_{\beta=0} = -\hat{\boldsymbol{n}}\hat{\boldsymbol{v}} \tag{B.8}$$

$$\left.\frac{d^2\mathcal{D}^{-1}}{d\beta^2}\right|_{\beta=0} = 1 \tag{B.9}$$

$$\left.\frac{d\bar{I}(\mathcal{D}^{-1}f)}{d(\mathcal{D}^{-1}f)}\right|_{\beta=0} = n_I \frac{\bar{I}(f)}{f} \tag{B.10}$$

$$\left.\frac{d^2\bar{I}(\mathcal{D}^{-1}f)}{d(\mathcal{D}^{-1}f)^2}\right|_{\beta=0} = \left(\alpha_I + n_I^2 + n_I\right)\frac{\bar{I}(f)}{f^2}, \tag{B.11}$$

where

$$\frac{d\ln\bar{I}}{d\ln f} \equiv n_I \tag{B.12}$$

$$\frac{dn_I}{d\ln f} \equiv \alpha_I. \tag{B.13}$$

Using these relations, equation (B.5) becomes

$$\begin{aligned}\frac{I(f,\hat{\boldsymbol{n}})}{\bar{I}(f)} = \mathcal{D}\frac{\bar{I}(\mathcal{D}^{-1}f)}{\bar{I}(f)} &= \left[1 - \frac{\beta^2}{6}(1 - n_I^2 - \alpha_I)\right] + \beta(1 - n_I)\hat{\boldsymbol{n}}\hat{\boldsymbol{v}} \\ &+ \frac{\beta^2}{2}\left((\hat{\boldsymbol{n}}\hat{\boldsymbol{v}})^2 - \frac{1}{3}\right)(2 - 3n_I + n_I^2 + \alpha_I) + \mathcal{O}(\beta^3).\end{aligned} \tag{B.14}$$

C

Model files

In this appendix, the model files for the two main analyses are provided. Other models only change slightly and can be easily reproduced from the code blocks provided here. The following model uses the solution for $\Gamma_{ab}^{(2)}$ provided in appendix A and derives its autocorrelation by taking $x_{ab} \to 0$.

```python
import numpy as np
import pickle
import ptarcade.models_utils as aux
from ptarcade.models_utils import prior
from enterprise import constants as const

name = "dipole_fixed_noAC_1"

smbhb = False

# A and gamma priors as in Evidence for a GWB paper
parameters = {
    "beta": prior("Uniform", 0, 1),
    "log10_A": prior("Uniform", -18, -11),
    "gamma": prior("Uniform", 0, 7)
}

alpha_vel = 167.942/360*2*np.pi
delta_vel = -6.944/360*2*np.pi
vel = np.array([np.cos(delta_vel)*np.cos(alpha_vel), np.cos(delta_vel)*np.sin(alpha_vel), np.sin(delta_vel)])

```

```python
def ORF_func(pos1, pos2, beta, n_I, vel):
    # Defining variables
    y_ab = (1-np.dot(pos1,pos2))/2

    # First, second and third order contributions
    first_Order = ((1/3)-(y_ab/6) + (y_ab*np.log(y_ab)))*(3/2)
    second_Order = ((1/12)+(y_ab/2)+(y_ab*np.log(y_ab)/(2*(1-y_ab))))*(np.dot(pos1,vel)+np.dot(pos2,vel))*(3/2)

    term1 = (1/4*y_ab**3 - y_ab**2 + 3/4*y_ab*np.log(y_ab) + 1/2*y_ab + 1/4) * (np.dot(pos1, vel)**2 + np.dot(pos2, vel)**2)
    term2 = (3/2*y_ab**2 * np.log(y_ab) - 39/20*y_ab**2 + 12/5*y_ab - 9/20) * (np.dot(pos1, vel) * np.dot(pos2, vel))
    term3 = y_ab**3*np.log(y_ab) - 22/15*y_ab**3 - 1/2*y_ab**2*np.log(y_ab) + 35/12*y_ab**2 - 1/2*y_ab*np.log(y_ab) - 43/30*y_ab - 1/60

    # Define third order
    third_Order = (term1 + term2 + term3)/(y_ab - 1)**2

    # Putting everything together setting alpha_I to zero
    return (1-beta**2/6*(1-n_I**2))*first_Order + beta*(n_I-1)*second_Order + beta**2/2*(2-3*n_I+n_I**2)*third_Order

def AC_func(pos1, beta, n_I, vel):

    first_Order = 1
    second_Order = 1/2*np.dot(pos1, vel)
    third_Order = 1/10*np.dot(pos1, vel)**2 - 1/30
```

```python

    # Putting everything together setting alpha_I to zero
    return (1-beta**2/6*(1-n_I**2))*first_Order + beta*(n_I-1)*second_Order + beta**2/2*(2-3*n_I+n_I**2)*third_Order


def orf(f, pos1, pos2, beta, log10_A, gamma):

    n_I = 2-gamma

    if np.all(pos1 == pos2):
        return AC_func(pos1=pos1, beta=beta, n_I=n_I, vel=vel)

    else:
        return ORF_func(pos1=pos1, pos2=pos2, beta=beta, n_I=n_I, vel=vel)

def spectrum(f, beta, log10_A, gamma):

    return 2*np.pi**2/3 * (aux.h/aux.H_0_Hz)**2 * (10 ** log10_A)** 2 * const.fyr**2 * (f/const.fyr)**(5 - gamma)
```

Afterwards, we consider the exact solution for Γ_{aa}, thus we make use of the pulsar distances which are imported in line 11/12 in the following model file.

```python
1 import numpy as np
2 import pickle
3 import ptarcade.models_utils as aux
4 from ptarcade.models_utils import prior
5 from enterprise import constants as const
6
7 name = "dipole_fixed_firstrun"
```

```

smbhb = False

with open('/home/m/mbluemke/dipole/dists.pkl', 'rb') as f:
    dists = pickle.load(f)
with open('/home/m/mbluemke/dipole/pos.pkl', 'rb') as f:
    pos = pickle.load(f)


#A and gamma priors as in Evidence for a GWB paper
parameters = {
    "beta": prior("Uniform", 0, 1),
    "log10_A": prior("Uniform", -18, -11),
    "gamma": prior("Uniform", 0, 7)
}


alpha_vel = 167.942/360*2*np.pi
delta_vel = -6.944/360*2*np.pi
vel = np.array([np.cos(delta_vel)*np.cos(alpha_vel), np.cos(delta_vel)*np.sin(alpha_vel), np.sin(delta_vel)])

for key, value in dists.items():
    parameters['dist_'+ key] = prior("TruncNormal", value[0], value[1], 0, 10)


def auto_corr(beta, freq, leng, n_I, pos, vel):
    #Defining variables
    y = np.pi*freq*leng

    fL= freq*leng

    #First and second order contributions
```

```
    first_Order = (1)-((3/8)*(1-np.sinc(4*y))/((y**2)))
    second_Order = ((-32 * y**4 + 48 * y**2 + 6 * y * np.sin(4 * y) + 9 * np.cos(4 * y) - 9) * np.dot(pos,vel)/(64 * y**4))
    third_Order = -3 / 16 * (
    np.pi * (-1 / (np.pi**2 * fL**2) + (3 / 2) / (np.pi**4 * fL**4)) * (1 - np.dot(pos, vel)**2)
    - 2 * np.pi * (-1 / (np.pi**2 * fL**2) + (3 / 2) / (np.pi**4 * fL**4)) * np.dot(pos, vel)**2
    - 2 * np.pi * ((3 / 4) / (np.pi**2 * fL**2) - (3 / 8) / (np.pi**4 * fL**4)) * (1 - np.dot(pos, vel)**2)
    + 4 * np.pi * ((3 / 4) / (np.pi**2 * fL**2) - (3 / 8) / (np.pi**4 * fL**4)) * np.dot(pos, vel)**2
    - 13 / 10 * np.pi * (1 - np.dot(pos, vel)**2)
    - 31 / 15 * np.pi * np.dot(pos, vel)**2
    + (1 / 2) * (1 - np.dot(pos, vel)**2) / (np.pi * fL**2)
    + np.dot(pos, vel)**2 / (np.pi * fL**2)
) / np.pi + (3 / 16) * (
    2 * np.pi * ((1 / 2) * np.sin(4 * np.pi * fL) / (np.pi * fL)
    + (1 / 4) * np.cos(4 * np.pi * fL) / (np.pi**2 * fL**2)) * (1 - np.dot(pos, vel)**2)
    - 2 * np.pi * ((1 / 2) * np.sin(4 * np.pi * fL) / (np.pi * fL)
    + (1 / 2) * np.cos(4 * np.pi * fL) / (np.pi**2 * fL**2)
    - (1 / 4) * np.sin(4 * np.pi * fL) / (np.pi**3 * fL**3)) * np.dot(pos, vel)**2
    - 2 * np.pi * ((1 / 2) * np.sin(4 * np.pi * fL) / (np.pi * fL)
    + (3 / 4) * np.cos(4 * np.pi * fL) / (np.pi**2 * fL**2)
```

```
    - (3 / 4) * np.sin(4 * np.pi * fL) / (np.pi**3 * fL**3)
    - (3 / 8) * np.cos(4 * np.pi * fL) / (np.pi**4 * fL**4)) * (1 - np.dot(pos, vel)**2)
    + 4 * np.pi * ((1 / 2) * np.sin(4 * np.pi * fL) / (np.pi * fL)
    + (3 / 4) * np.cos(4 * np.pi * fL) / (np.pi**2 * fL**2)
    - (3 / 4) * np.sin(4 * np.pi * fL) / (np.pi**3 * fL**3)
    - (3 / 8) * np.cos(4 * np.pi * fL) / (np.pi**4 * fL**4)) * np.dot(pos, vel)**2
    + np.pi * ((1 / 2) * np.sin(4 * np.pi * fL) / (np.pi * fL)
    + np.cos(4 * np.pi * fL) / (np.pi**2 * fL**2)
    - (3 / 2) * np.sin(4 * np.pi * fL) / (np.pi**3 * fL**3)
    - (3 / 2) * np.cos(4 * np.pi * fL) / (np.pi**4 * fL**4)
    + (3 / 4) * np.sin(4 * np.pi * fL) / (np.pi**5 * fL**5)) * (1 - np.dot(pos, vel)**2)
    - 2 * np.pi * ((1 / 2) * np.sin(4 * np.pi * fL) / (np.pi * fL)
    + np.cos(4 * np.pi * fL) / (np.pi**2 * fL**2)
    - (3 / 2) * np.sin(4 * np.pi * fL) / (np.pi**3 * fL**3)
    - (3 / 2) * np.cos(4 * np.pi * fL) / (np.pi**4 * fL**4)
    + (3 / 4) * np.sin(4 * np.pi * fL) / (np.pi**5 * fL**5)) * np.dot(pos, vel)**2
    + (3 / 10) * np.pi * (1 - np.dot(pos, vel)**2)
    + (1 / 15) * np.pi * np.dot(pos, vel)**2
    - (1 / 2) * (1 - np.dot(pos, vel)**2) * np.sin(4 * np.pi * fL) / fL
```

```python
) / np.pi - 1 / 3 + 0.125 / (np.pi**2 * fL**2) - 0.03125 * np.sin(4 * np.pi * fL) / (np.pi**3 * fL**3)

    return (1 - beta**2/6*(1 - n_I**2))*first_Order + beta*(1 - n_I)*second_Order + beta**2/2*(2 - 3*n_I + n_I**2)*third_Order

def ORF_func(pos1, pos2, beta, n_I, vel):
    # Defining variables
    y_ab = (1-np.dot(pos1,pos2))/2

    # First, second and third order contributions
    first_Order = ((1/3)-(y_ab/6) + (y_ab*np.log(y_ab)))*(3/2)
    second_Order = ((1/12)+(y_ab/2)+(y_ab*np.log(y_ab)/(2*(1-y_ab))))*(np.dot(pos1,vel)+np.dot(pos2,vel))*(3/2)

    term1 = (1/4*y_ab**3 - y_ab**2 + 3/4*y_ab*np.log(y_ab) + 1/2*y_ab + 1/4) * (np.dot(pos1, vel)**2 + np.dot(pos2, vel)**2)
    term2 = (3/2*y_ab**2 * np.log(y_ab) - 39/20*y_ab**2 + 12/5*y_ab - 9/20) * (np.dot(pos1, vel) * np.dot(pos2, vel))
    term3 = y_ab**3*np.log(y_ab) - 22/15*y_ab**3 - 1/2*y_ab**2*np.log(y_ab) + 35/12*y_ab**2 - 1/2*y_ab*np.log(y_ab) - 43/30*y_ab - 1/60

    # Define third order
    third_Order = (term1 + term2 + term3)/(y_ab - 1)**2

    # Putting everything together setting alpha_I to zero
```

```
    return (1-beta**2/6*(1-n_I**2))*first_Order + beta*(
        n_I-1)*second_Order + beta**2/2*(2-3*n_I+n_I**2)*
        third_Order

def orf(f, pos1, pos2, beta, log10_A, gamma,
    dist_J0613m0200, dist_J2234p0611, dist_J1713p0747,
    dist_J1455m3330, dist_J0557p1551, dist_J1614m2230,
    dist_J1640p2224, dist_J1643m1224, dist_J1944p0907,
    dist_J1744m1134, dist_J2124m3358, dist_J1719m1438,
    dist_J0740p6620, dist_J1738p0333, dist_J0340p4130,
    dist_J1600m3053, dist_J0509p0856,
            dist_J2043p1711, dist_J0645p5158, dist_J2302p4442
                , dist_J2229p2643, dist_J1923p2515,
                dist_J1909m3744, dist_J2214p3000,
                dist_J0614m3329, dist_B1953p29, dist_J0406p3039
                , dist_J1453p1902, dist_J1751m2857,
                dist_B1855p09, dist_J1022p1001, dist_J2317p1439
                , dist_J1911p1347, dist_J0931m1902,
                dist_J2033p1734, dist_J1630p3734,
                dist_J1741p1351,
            dist_J1730m2304, dist_J0605p3757, dist_J1802m2124
                , dist_J1843m1113, dist_J1312p0051,
                dist_J2010m1323, dist_J1125p7819,
                dist_J0023p0923, dist_J1910p1256,
                dist_J1745p1017, dist_J1946p3417,
                dist_J1012p5307, dist_J2322p2057,
                dist_J0437m4715, dist_J2017p0603,
                dist_J0709p0458, dist_J1024m0719,
                dist_J1918m0642, dist_J0030p0451,
                dist_J2145m0750,
```

```
         dist_J1012m4235, dist_J1811m2405, dist_J0636p5128
            , dist_J2234p0944, dist_J1903p0327,
            dist_J1705m1903, dist_B1937p21, dist_J1747m4036
            , dist_J0610m2100, dist_J1853p1303,
            dist_J1832m0836):

    n_I = 2-gamma
    kpc_to_sec = 102927125054.33899

    if np.all(pos1 == pos2):
        dist = locals()['dist_' + pos[pos1[0]]] *
           kpc_to_sec
        return auto_corr(beta=beta, freq=f, leng=dist, n_I
           =n_I, pos=pos1, vel=vel)

    else:
        return ORF_func(pos1=pos1, pos2=pos2, beta=beta,
           n_I=n_I, vel=vel)

def spectrum(f, beta, log10_A, gamma, dist_J0613m0200,
   dist_J2234p0611, dist_J1713p0747, dist_J1455m3330,
   dist_J0557p1551, dist_J1614m2230, dist_J1640p2224,
   dist_J1643m1224, dist_J1944p0907, dist_J1744m1134,
   dist_J2124m3358, dist_J1719m1438, dist_J0740p6620,
   dist_J1738p0333, dist_J0340p4130, dist_J1600m3053,
   dist_J0509p0856,
```

```
         dist_J2043p1711, dist_J0645p5158, dist_J2302p4442
            , dist_J2229p2643, dist_J1923p2515,
            dist_J1909m3744, dist_J2214p3000,
            dist_J0614m3329, dist_B1953p29, dist_J0406p3039
            , dist_J1453p1902, dist_J1751m2857,
            dist_B1855p09, dist_J1022p1001, dist_J2317p1439
            , dist_J1911p1347, dist_J0931m1902,
            dist_J2033p1734, dist_J1630p3734,
            dist_J1741p1351,
         dist_J1730m2304, dist_J0605p3757, dist_J1802m2124
            , dist_J1843m1113, dist_J1312p0051,
            dist_J2010m1323, dist_J1125p7819,
            dist_J0023p0923, dist_J1910p1256,
            dist_J1745p1017, dist_J1946p3417,
            dist_J1012p5307, dist_J2322p2057,
            dist_J0437m4715, dist_J2017p0603,
            dist_J0709p0458, dist_J1024m0719,
            dist_J1918m0642, dist_J0030p0451,
            dist_J2145m0750,
         dist_J1012m4235, dist_J1811m2405, dist_J0636p5128
            , dist_J2234p0944, dist_J1903p0327,
            dist_J1705m1903, dist_B1937p21, dist_J1747m4036
            , dist_J0610m2100, dist_J1853p1303,
            dist_J1832m0836):

    return 2*np.pi**2/3 * (aux.h/aux.H_0_Hz)**2 * (10 **
       log10_A)** 2 * const.fyr**2 * (f/const.fyr)**(5 -
       gamma)
```

Bibliography

[1] Gabriella Agazie et al. “The NANOGrav 15-year Data Set: Evidence for a Gravitational-Wave Background”. In: *The Astrophysical Journal Letters* 951.1 (July 1, 2023), p. L8. ISSN: 2041-8205, 2041-8213. DOI: 10.3847/2041-8213/acdac6. arXiv: 2306.16213 [astro-ph]. URL: http://arxiv.org/abs/2306.16213 (visited on 04/14/2025).

[2] Gabriella Agazie et al. *The NANOGrav 15-year Data Set: Search for Anisotropy in the Gravitational-Wave Background*. June 28, 2023. DOI: 10.48550/arXiv.2306.16221. arXiv: 2306.16221 [astro-ph]. URL: http://arxiv.org/abs/2306.16221 (visited on 06/05/2025).

[3] N. M. Jiménez Cruz et al. *Measuring kinematic anisotropies with pulsar timing arrays*. June 7, 2024. DOI: 10.48550/arXiv.2402.17312. arXiv: 2402.17312 [gr-qc]. URL: http://arxiv.org/abs/2402.17312 (visited on 03/18/2025).

[4] Planck Collaboration et al. “*Planck* 2018 results: I. Overview and the cosmological legacy of *Planck*”. In: *Astronomy & Astrophysics* 641 (Sept. 2020), A1. ISSN: 0004-6361, 1432-0746. DOI: 10.1051/0004-6361/201833880. URL: https://www.aanda.org/10.1051/0004-6361/201833880 (visited on 05/19/2025).

[5] Nina Cordes et al. *On the overlap reduction function of pulsar timing array searches for gravitational waves in modified gravity*. Jan. 31, 2025. DOI: 10.48550/arXiv.2407.04464. arXiv: 2407.04464 [gr-qc]. URL: http://arxiv.org/abs/2407.04464 (visited on 03/18/2025).

[6] Jorge Pinochet. “General relativity in a nutshell I”. In: *Physica Scripta* 98.12 (Dec. 1, 2023), p. 126103. ISSN: 0031-8949, 1402-4896. DOI: `10.1088/1402-4896/ad0c34`. arXiv: `2401.08612[physics]`. URL: `http://arxiv.org/abs/2401.08612` (visited on 03/25/2025).

[7] Jorge Pinochet. “General relativity in a nutshell II”. In: *Physica Scripta* 98.12 (Dec. 1, 2023), p. 126104. ISSN: 0031-8949, 1402-4896. DOI: `10.1088/1402-4896/ad0c15`. arXiv: `2401.12219[physics]`. URL: `http://arxiv.org/abs/2401.12219` (visited on 03/25/2025).

[8] Michele Maggiore. *Gravitational Waves: Volume 1: Theory and Experiments*. 1st ed. Oxford University PressOxford, Oct. 4, 2007. ISBN: 978-0-19-857074-5. DOI: `10.1093/acprof:oso/9780198570745.001.0001`. URL: `https://academic.oup.com/book/41655` (visited on 03/26/2025).

[9] Stephen R. Taylor. *The Nanohertz Gravitational Wave Astronomer*. May 27, 2021. DOI: `10.48550/arXiv.2105.13270`. arXiv: `2105.13270[astro-ph]`. URL: `http://arxiv.org/abs/2105.13270` (visited on 03/25/2025).

[10] Glauber C. Dorsch and Lucas E. A. Porto. “An introduction to gravitational waves through electrodynamics: a quadrupole comparison”. In: *European Journal of Physics* 43.2 (Mar. 1, 2022), p. 025602. ISSN: 0143-0807, 1361-6404. DOI: `10.1088/1361-6404/ac4645`. arXiv: `2201.06722[gr-qc]`. URL: `http://arxiv.org/abs/2201.06722` (visited on 03/27/2025).

[11] Nigel T. Bishop and Luciano Rezzolla. “Extraction of Gravitational Waves in Numerical Relativity”. In: *Living Reviews in Relativity* 19.1 (Dec. 2016), p. 2. ISSN: 2367-3613, 1433-8351. DOI: `10.1007/s41114-016-0001-9`. arXiv: `1606.02532[gr-qc]`. URL: `http://arxiv.org/abs/1606.02532` (visited on 03/28/2025).

[12] Joseph D. Romano and Neil J. Cornish. “Detection methods for stochastic gravitational-wave backgrounds: a unified treatment”. In: *Living Reviews in Relativity* 20.1 (Dec. 2017), p. 2. ISSN: 2367-3613, 1433-8351. DOI: `10.1007/s41114-017-0004-1`. arXiv: `1608.06889[gr-qc]`. URL: `http://arxiv.org/abs/1608.06889` (visited on 04/03/2025).

[13] A. G. Lyne and Francis Graham-Smith. *Pulsar astronomy*. 4th ed. Cambridge astrophysics 48. Cambridge ; New York: Cambridge University Press, 2012. 345 pp. ISBN: 978-1-107-01014-7.

[14] Giulia Cusin and Gianmassimo Tasinato. “Doppler boosting the stochastic gravitational wave background”. In: *Journal of Cosmology and Astroparticle Physics* 2022.8 (Aug. 1, 2022), p. 036. ISSN: 1475-7516. DOI: `10.1088/1475-7516/2022/08/036`. arXiv: `2201.10464[astro-ph]`. URL: `http://arxiv.org/abs/2201.10464` (visited on 03/18/2025).

[15] Gianmassimo Tasinato. *Kinematic anisotropies and pulsar timing arrays*. Nov. 30, 2023. DOI: `10.48550/arXiv.2309.00403`. arXiv: `2309.00403[gr-qc]`. URL: `http://arxiv.org/abs/2309.00403` (visited on 03/18/2025).

[16] Michele Maggiore. *Gravitational Waves: Volume 2: Astrophysics and Cosmology*. 1st ed. Oxford University PressOxford, Mar. 22, 2018. ISBN: 978-0-19-181718-2. DOI: `10.1093/oso/9780198570899.001.0001`. URL: `https://academic.oup.com/book/43950` (visited on 04/04/2025).

[17] Joseph D. Romano and Bruce Allen. “Answers to frequently asked questions about the pulsar timing array Hellings and Downs curve”. In: *Classical and Quantum Gravity* 41.17 (Sept. 5, 2024), p. 175008. ISSN: 0264-9381, 1361-6382. DOI: `10.1088/1361-6382/ad4c4c`. arXiv: `2308.05847[gr-qc]`. URL: `http://arxiv.org/abs/2308.05847` (visited on 03/18/2025).

[18] Adrian Ka-Wai Chung et al. “Targeted search for the kinematic dipole of the gravitational-wave background”. In: *Physical Review D* 106.8 (Oct. 21, 2022), p. 082005. ISSN: 2470-0010, 2470-0029. DOI: `10.1103/PhysRevD.106.082005`. arXiv: `2208.01330[gr-qc]`. URL: `http://arxiv.org/abs/2208.01330` (visited on 04/29/2025).

[19] John M. McKinley. “Relativistic transformations of light power”. In: *American Journal of Physics* 47.7 (July 1, 1979), pp. 602–605. ISSN: 0002-9505, 1943-2909. DOI: `10.1119/1.11762`. URL: `https://pubs.aip.org/ajp/article/47/7/602/1051215/Relativistic-transformations-of-light-power` (visited on 06/04/2025).

[20] Fredrick A. Jenet and Joseph D. Romano. *Understanding the gravitational-wave Hellings and Downs curve for pulsar timing arrays in terms of sound and electromagnetic waves*. Mar. 27, 2015. DOI: `10.48550/arXiv.1412.1142`. arXiv: `1412.1142[gr-qc]`. URL: `http://arxiv.org/abs/1412.1142` (visited on 03/18/2025).

[21] R. N. Manchester et al. “The ATNF Pulsar Catalogue”. In: *The Astronomical Journal* 129.4 (Apr. 2005), pp. 1993–2006. ISSN: 0004-6256, 1538-3881. DOI: `10.1086/428488`. arXiv: `astro-ph/0412641`. URL: `http://arxiv.org/abs/astro-ph/0412641` (visited on 05/29/2025).

[22] Robert D. Cousins. “Why isn’t every physicist a Bayesian?” In: *American Journal of Physics* 63.5 (May 1, 1995), pp. 398–410. ISSN: 0002-9505, 1943-2909. DOI: `10.1119/1.17901`. URL: `https://pubs.aip.org/ajp/article/63/5/398/1054660/Why-isn-t-every-physicist-a-Bayesian` (visited on 06/23/2025).

[23] Andrea Mitridate et al. *PTArcade*. June 28, 2023. DOI: `10.48550/arXiv.2306.16377`. arXiv: `2306.16377[hep-ph]`. URL: `http://arxiv.org/abs/2306.16377` (visited on 03/25/2025).

[24] M. Vallisneri et al. “Modeling the uncertainties of solar-system ephemerides for robust gravitational-wave searches with pulsar timing arrays”. In: *The Astrophysical Journal* 893.2 (Apr. 1, 2020), p. 112. ISSN: 0004-637X, 1538-4357. DOI: `10.3847/1538-4357/ab7b67`. arXiv: `2001.00595[astro-ph]`. URL: `http://arxiv.org/abs/2001.00595` (visited on 06/15/2025).

[25] Bruce Allen and Joseph D. Romano. “Detecting a stochastic background of gravitational radiation: Signal processing strategies and sensitivities”. In: *Physical Review D* 59.10 (Mar. 31, 1999), p. 102001. ISSN: 0556-2821, 1089-4918. DOI: `10.1103/PhysRevD.59.102001`. arXiv: `gr-qc/9710117`. URL: `http://arxiv.org/abs/gr-qc/9710117` (visited on 06/15/2025).

[26] Lindley Lentati et al. “Hyper-efficient model-independent Bayesian method for the analysis of pulsar timing data”. In: *Physical Review D* 87.10 (May 20, 2013), p. 104021. ISSN: 1550-7998, 1550-2368. DOI: `10.1103/PhysRevD.87.104021`. arXiv: `1210.3578[astro-ph]`. URL: `http://arxiv.org/abs/1210.3578` (visited on 06/15/2025).

[27] Rutger Van Haasteren and Yuri Levin. “Understanding and analysing time-correlated stochastic signals in pulsar timing”. In: *Monthly Notices of the Royal Astronomical Society* 428.2 (Jan. 11, 2013), pp. 1147–1159. ISSN: 1365-2966, 0035-8711. DOI: `10.1093/mnras/sts097`. URL: `http://academic.oup.com/mnras/article/428/2/1147/1000366/Understanding-and-analysing-timecorrelated` (visited on 06/15/2025).

[28] Andrea Mitridate. *PTArcade*. In collab. with Andrea Mitridate and David Wright. Version v0.0.0. Apr. 28, 2023. DOI: `10.5281/ZENODO.7876430`. URL: `https://zenodo.org/record/7876430` (visited on 03/25/2025).

[29] Justin A. Ellis et al. *ENTERPRISE: Enhanced Numerical Toolbox Enabling a Robust PulsaR Inference SuitE*. Version v3.0.0. Sept. 29, 2020. DOI: `10.5281/ZENODO.4059815`. URL: `https://zenodo.org/record/4059815` (visited on 03/25/2025).

[30] Stephen R. Taylor et al. *enterprise_extensions*. 2021. URL: `https://github.com/nanograv/enterprise_extensions`.

[31] The NANOGrav Collaboration. *The NANOGrav 15-Year Data Set*. In collab. with Joseph K. Swiggum, H. Thankful Cromartie, and Joseph Glaser. Version 2.0.1. Jan. 30, 2025. DOI: `10.5281/ZENODO.7967584`. URL: `https://zenodo.org/doi/10.5281/zenodo.7967584` (visited on 05/28/2025).

[32] Adeela Afzal et al. "The NANOGrav 15-year Data Set: Search for Signals from New Physics". In: *The Astrophysical Journal Letters* 951.1 (July 1, 2023), p. L11. ISSN: 2041-8205, 2041-8213. DOI: `10.3847/2041-8213/acdc91`. arXiv: `2306.16219[astro-ph]`. URL: `http://arxiv.org/abs/2306.16219` (visited on 05/28/2025).

[33] Gabriella Agazie et al. "The NANOGrav 15-year Data Set: Constraints on Supermassive Black Hole Binaries from the Gravitational Wave Background". In: *The Astrophysical Journal Letters* 952.2 (Aug. 1, 2023), p. L37. ISSN: 2041-8205, 2041-8213. DOI: `10.3847/2041-8213/ace18b`. arXiv: `2306.16220[astro-ph]`. URL: `http://arxiv.org/abs/2306.16220` (visited on 05/28/2025).

[34] Aaron Johnson et al. *NANOGrav_15yr_tutorial*. 2023. URL: `https://github.com/nanograv/15yr_stochastic_analysis` (visited on 05/28/2025).

[35] Chiara M. F. Mingarelli et al. "The local nanohertz gravitational-wave landscape from supermassive black hole binaries". In: *Nature Astronomy* 1.12 (Nov. 13, 2017), pp. 886–892. ISSN: 2397-3366. DOI: `10.1038/s41550-017-0299-6`. URL: `https://www.nature.com/articles/s41550-017-0299-6` (visited on 06/07/2025).

[36] Bruce Allen and Adrian C. Ottewill. “Detection of anisotropies in the gravitational-wave stochastic background”. In: *Physical Review D* 56.2 (July 15, 1997), pp. 545–563. ISSN: 0556-2821, 1089-4918. DOI: `10.1103/PhysRevD.56.545`. URL: `https://link.aps.org/doi/10.1103/PhysRevD.56.545` (visited on 06/07/2025).

[37] Paul Frederik Depta et al. *Pulsar timing array sensitivity to anisotropies in the gravitational wave background*. Aug. 30, 2024. DOI: `10.48550/arXiv.2407.14460`. arXiv: `2407.14460[astro-ph]`. URL: `http://arxiv.org/abs/2407.14460` (visited on 06/07/2025).

[38] Stephen R. Taylor and Jonathan R. Gair. “Searching For Anisotropic Gravitational-wave Backgrounds Using Pulsar Timing Arrays”. In: *Physical Review D* 88.8 (Oct. 1, 2013), p. 084001. ISSN: 1550-7998, 1550-2368. DOI: `10.1103/PhysRevD.88.084001`. arXiv: `1306.5395[gr-qc]`. URL: `http://arxiv.org/abs/1306.5395` (visited on 06/08/2025).

[39] Emiko C. Gardiner et al. *Beyond the Background: Gravitational Wave Anisotropy and Continuous Waves from Supermassive Black Hole Binaries*. Apr. 23, 2024. DOI: `10.48550/arXiv.2309.07227`. arXiv: `2309.07227[astro-ph]`. URL: `http://arxiv.org/abs/2309.07227` (visited on 06/08/2025).

[40] Thomas Konstandin et al. *The impact of cosmic variance on PTAs anisotropy searches*. June 2, 2025. DOI: `10.48550/arXiv.2408.07741`. arXiv: `2408.07741[astro-ph]`. URL: `http://arxiv.org/abs/2408.07741` (visited on 06/08/2025).

[41] Nicola Bartolo et al. “Science with the space-based interferometer LISA. IV: Probing inflation with gravitational waves”. In: *Journal of Cosmology and Astroparticle Physics* 2016.12 (Dec. 14, 2016), pp. 026–026. ISSN: 1475-7516. DOI: `10.1088/1475-7516/2016/12/026`. arXiv: `1610.06481[astro-ph]`. URL: `http://arxiv.org/abs/1610.06481` (visited on 06/09/2025).

[42] Giorgio Mentasti, Carlo R. Contaldi, and Marco Peloso. *Strong scale-dependence does not enhance the kinematic boosting of gravitational wave backgrounds*. July 22, 2025. DOI: `10.48550/arXiv.2507.16901`. arXiv: `2507.16901[astro-ph]`. URL: `http://arxiv.org/abs/2507.16901` (visited on 07/28/2025).

[43] Nathan Secrest et al. *Colloquium: The Cosmic Dipole Anomaly*. Version Number: 1. 2025. DOI: `10.48550/ARXIV.2505.23526`. URL: `https://arxiv.org/abs/2505.23526` (visited on 06/09/2025).

[44] Melissa Anholm et al. “Optimal strategies for gravitational wave stochastic background searches in pulsar timing data”. In: *Physical Review D* 79.8 (Apr. 21, 2009), p. 084030. ISSN: 1550-7998, 1550-2368. DOI: `10.1103/PhysRevD.79.084030`. arXiv: `0809.0701 [gr-qc]`. URL: `http://arxiv.org/abs/0809.0701` (visited on 03/19/2025).

Acknowlegement

Calculations (or parts of them) for this publication were performed on the HPC cluster PALMA II of the University of Münster, subsidised by the DFG (INST 211/667-1). Help with the implementation was also provided by Andrea Mitridate and David Wright. We acknowledge the productive exchange with the authors Tasinato et al., whose paper this Bachelor thesis is based on, for providing us with valuable insights that enabled us to reproduce and build upon their results. On a more personal note, I want to especially thank my co-supervisor Tobias Schröder for his help and contributions to the project (all that while suffering through his PhD writing phase) and Kai Schmitz for his guidance and input. My gratitude also extends to all members of PCM, who allowed me to write my Bachelor's thesis in a very welcoming environment.